

Phase state and viscosity of secondary organic aerosols over China simulated by WRF-Chem

Zhiqiang Zhang^{1,2}, Ying Li¹, Haiyan Ran^{1,2}, Junling An¹, Yu Qu¹, Wei Zhou¹, Weiqi Xu¹, Weiwei Hu³, Hongbin Xie⁴, Zifa Wang¹, Yele Sun¹, Manabu Shiraiwa⁵

¹State Key Laboratory of Atmospheric Boundary Layer Physics and Atmospheric Chemistry, Institute of Atmospheric Physics, Chinese Academy of Sciences, Beijing 100029, China

²College of Earth and Planetary Sciences, University of Chinese Academy of Sciences, Beijing 100049, China

³State Key Laboratory of Organic Geochemistry, Guangzhou Institute of Geochemistry, Chinese Academy of Sciences, Guangzhou 510640, China

⁴Key Laboratory of Industrial Ecology and Environmental Engineering (Ministry of Education), School of Environmental Science and Technology, Dalian University of Technology, Dalian 116024, China

⁵Department of Chemistry, University of California, Irvine, CA 92697-2025, USA

Correspondence to: Ying Li (liying-iap@mail.iap.ac.cn)

Abstract. Secondary organic aerosols (SOA) can exist in liquid, semi-solid or amorphous solid states, which are rarely accounted for in current chemical transport models (CTMs). Missing the information of SOA phase state and viscosity in CTMs impedes accurate representation of SOA formation and evolution, affecting the predictions of aerosol effects on air quality and climate. We have previously developed a [parameterization](#) to estimate the glass transition temperature (T_g) of an organic compound based on volatility [and to predict viscosity of SOA](#). In this study, we apply this method to predict the phase state of SOA particles over China in summer of 2018 using the Weather Research and Forecasting model coupled to Chemistry (WRF-Chem). This is the first time that spatial distributions of the SOA phase state over China are investigated by a regional CTM. Simulations show that T_g values of dry SOA range from ~287 K to 305 K, with higher values in the northwestern China where SOA particles have larger mass fractions of low volatility compounds. Considering water uptake by SOA particles, the SOA viscosity shows a prominent geospatial gradient that highly viscous or solid SOA particles are mainly [predicted](#) in the northwestern China. The lowest and highest SOA viscosity values both occur over the Qinghai-Tibet Plateau that the solid phase state is predicted over dry and high-altitude areas and the liquid phase state is predicted mainly in the south of the plateau with high relative humidity during the summer monsoon season. [We also calculate](#) the characteristic mixing timescale of organic molecules in 200 nm SOA particles [to evaluate kinetic limitations in SOA partitioning](#). Calculations show that during the simulated period the percent time of the mixing timescale longer than 1 h is > 70 % at the surface and at 500 hPa in most areas of the northern China, indicating that kinetic partitioning considering the bulk diffusion in viscous particles may be required for more accurate prediction of SOA mass concentrations and size distributions over these areas. Sensitivity simulations show that including the formation of extremely low-volatile organic compounds, the percent time that a SOA particle is in the liquid phase state decreases by up to 12 % in the southeastern China during the

33 simulated period. With an assumption that the organic and inorganic compounds are internally mixed in one phase, we show
34 that the water absorbed by inorganic species can significantly lower the simulated viscosity over the southeastern China.
35 This indicates that constraining the uncertainties in simulated SOA volatility distributions and [the mixing state of the organic](#)
36 [and inorganic compounds](#) would improve prediction of viscosity in multicomponent particles in southeastern China.

37 **1 Introduction**

38 Secondary organic aerosols (SOA) are major components of atmospheric fine particles, impacting air quality, climate and
39 public health (Jimenez et al., 2009; Pöschl and Shiraiwa, 2015). The formation and evolution of SOA involve both chemical
40 reactions and mass transport in the gas and particle phases (Ziemann and Atkinson, 2012). This complexity makes accurate
41 representation of SOA evolution in chemical transport models (CTMs) challenging, leading to a large uncertainty in
42 evaluating SOA impacts on air quality and climate (Kanakidou et al., 2005; Shrivastava et al., 2017).

43 Current CTMs usually assume that SOA particles are homogeneous and well-mixed liquids, with rapid establishment of
44 gas-particle equilibrium applied in simulations of SOA formation and partitioning (Pankow, 1994; Donahue et al., 2006). It
45 has been shown that SOA can exist in liquid (low dynamic viscosity η , $\eta < 10^2$ Pa s), semi-solid (10^2 Pa s $\leq \eta \leq 10^{12}$ Pa s) or
46 solid (amorphous or glassy solid; $\eta > 10^{12}$ Pa s) states, depending on particle chemical composition and atmospheric
47 conditions, such as ambient temperature (T) and relative humidity (RH) (Koop et al., 2011; Reid et al., 2018). Viscosities can
48 be converted to bulk diffusion coefficients via the Stokes-Einstein equation (Einstein, 1905; Seinfeld and Pandis, 2016) or
49 the fractional Stokes-Einstein equation (Price et al., 2016; Evoy et al., 2019; Evoy et al., 2020). The phase state, viscosity,
50 and bulk diffusivity of SOA are important in many aerosol processes. The semi-solid or solid phase state can prolong the
51 equilibration timescales in the gas-particle partitioning, indicating a need of considering kinetic limitations in [simulating](#) the
52 SOA partitioning into highly viscous particles (Shiraiwa and Seinfeld, 2012; Roldin et al., 2014; Zaveri et al., 2014; Li and
53 Shiraiwa, 2019). The viscosity of SOA can impact the rates of heterogeneous and multiphase reactions (Marshall et al., 2018;
54 Zhang et al., 2019a), photochemistry (Liu et al., 2018; Dalton and Nizkorodov, 2021; Baboosian et al., 2022), and the
55 uptake of gaseous pollutants (e.g., O₃, OH, N₂O₅, NO₂, NH₃, and SO₂) and water vapor (Abbatt et al., 2012; Kuwata and
56 Martin, 2012; Preston and Zuend, 2022), with implications for accurate predictions of atmospheric chemical composition
57 (Reid et al., 2018). The SOA phase state also affects particle size distribution evolution (Shiraiwa et al., 2013; [Zaveri et al.,](#)
58 [2022](#)) and ice nucleation pathways (Knopf and Alpert, 2023).

59 Accurate predictions of the viscosity need the information of molecular structures and functional groups (Song et al.,
60 2016; Rothfuss and Petters, 2017; Gervasi et al., 2020; Galeazzo and Shiraiwa, 2022); however, molecular specificity is
61 often [unavailable](#) in ambient measurements, [leading to the prediction of the phase state of ambient SOA particles difficult.](#)
62 Currently there are only a few methods developed to predict the phase state of ambient SOA particles, and successfully be

63 implemented in CTMs. Li, Shiraiwa and coauthors first developed a parameterization predicting the glass transition
64 temperature (T_g) based on the molar mass (M) and the atomic O/C ratio for carbon-hydrogen (CH) and
65 carbon-hydrogen-oxygen (CHO) compounds with their molar mass less than 450 g mol^{-1} (Shiraiwa et al., 2017). T_g
66 characterizes the temperature at which a phase transition between amorphous solid and semi-solid states occurs (Koop et al.,
67 2011). When the ambient T is higher than T_g , a SOA particle is in a semi-solid or liquid phase state; otherwise, it behaves as
68 an amorphous solid. This parameterization has been successfully coupled into CTMs simulating the SOA phase state over
69 the globe (Shiraiwa et al., 2017) or the U.S. (Schmedding et al., 2020; Li et al., 2021b), showing that semi-solid and
70 amorphous solid phase states frequently occurred over dry lands and in the upper troposphere. Further parameterizations
71 were developed to predict T_g as a function of the saturation mass concentration (C^0) and the O/C ratio of organic compounds,
72 or as a function of C^0 solely, which indirectly included the effect of molecular structure on T_g estimations (Li et al., 2020).
73 This parameterization can be used in the volatility basis set (VBS) framework (Donahue et al., 2006), which is widely
74 adopted in CMTs simulating SOA formation (Lane et al., 2008a; Knote et al., 2015). Rasool et al. (2021) then coupled this
75 new method (Li et al., 2020) into the Weather Research and Forecasting Model coupled to chemistry (WRF-Chem) (Grell et
76 al., 2005; Fast et al., 2006), and the simulations showed that the viscosity of SOA particles could be reasonably predicted
77 during the dry-to-wet transition season in the Amazon rainforest. Li et al. (2020) was also applied in the WRF-Chem
78 simulating the effects of particle phase state on the multiphase chemistry of SOA formation in the Amazon rainforest
79 (Shrivastava et al., 2022; Rasool et al., 2023). Instead of predicting T_g , Maclean et al. (2021) developed parameterizations for
80 viscosity as a function of T and RH based on measured viscosity data of laboratory SOA, and applied the viscosity
81 parameterizations in CTMs to predict the mixing timescales of organic molecules and water molecules within SOA particles
82 on a global scale (Maclean et al., 2017; Maclean et al., 2021). It is needed to conduct more simulations to investigate the
83 SOA phase state varied with locations and the time. Simulations of the SOA phase state in China on a regional scale have not
84 been available.

85 Investigations in the particle phase state over China are currently focused on field observations and laboratory
86 experiments. Bounce factor measurements showed that submicrometer particles can be semi-solid in clear days and liquid in
87 hazy days in Beijing, China (Liu et al., 2017). The phase state of $\text{PM}_{2.5}$ (particulate matter with an aerodynamic diameter \leq
88 $2.5 \mu\text{m}$) was found to be mostly semisolid to solid in winter Beijing based on the measurements using optical microscopy
89 combined with the poke-and-flow technique (Song et al., 2022). The RH-dependent viscosity of the proxies of actual
90 ambient particles in Beijing was also investigated based on dual optical tweezers (Tong et al., 2022). The phase state of
91 submicrometer particles in Beijing was retrieved from a polarization lidar that has the potential to infer the vertical profiles
92 of phase state (Tan et al., 2020). The phase state of traffic-related secondary aerosols in Beijing may have a distinguished
93 diurnal variation (Meng et al., 2021). The biomass burning aerosols, collected near a farmland in Yangtze River Delta, China,
94 were found to exist in the non-solid phase state at relatively dry conditions (Liu et al., 2021).

95 These measurements indicate that the particle phase state over China is highly variable under different atmospheric
96 conditions. It is important to know the spatial distributions and time variations of the SOA phase state and viscosity in
97 multicomponent particles to better quantify the aerosol effects on air quality, which, however, has not been investigated over
98 China with air quality models on a regional scale. Here we use the WRF-Chem model simulated SOA volatility distributions
99 to estimate the glass transition temperature and viscosity of SOA particles over China based on the parameterizations
100 developed in Li et al. (2020). We further calculate the diffusion coefficients and mixing timescales of organic molecules
101 within SOA, which has implications in how to properly treat the SOA partitioning (instantaneous equilibrium vs. kinetic
102 partitioning) in CTMs. As volatility and viscosity are closely related, we conduct a sensitivity calculation to evaluate the
103 effects of the simulated SOA volatility distributions on viscosity estimations. We also conduct a sensitivity calculation to
104 investigate how the water absorbed by inorganic components in PM_{2.5} affects viscosity estimations, which has implications
105 in predicting the viscosity of internally mixed ambient particles.

106 **2 Methods**

107 **2.1 WRF-Chem model configuration**

108 We use the WRF-Chem model version 3.7.1 (Grell et al., 2005; Fast et al., 2006) and simulate the period from 20 May to 23
109 June 2018 with a spin-up period of 7 days (May 13 – 19). We set up two domains (Fig. S1 in the Supplement) with the
110 horizontal resolutions of 81 km and 27 km, respectively, and 18 vertical layers are applied from the surface up to 100 hPa.
111 The meteorological initial and boundary conditions are from the National Centers for Environmental Prediction (NCEP)
112 Global Forecast System (GFS) final (FNL) reanalysis data. The outputs of a global chemical transport model MOZART-4
113 (Emmons et al., 2010) provide initial and boundary conditions of chemical species over the outer domain (Fig. S1 in the
114 Supplement). Anthropogenic emissions are from the MIX 2010 inventory for Asia (Li et al., 2017) and the MEIC 2016
115 inventory for China (<http://meicmodel.org.cn>) (Zheng et al., 2018). Biogenic emissions are calculated from the Model of
116 Emissions of Gases and Aerosols from Nature (MEGAN2.1) (Guenther et al., 2012).

117 The utilized physical and chemical schemes are given in Table S1. We use the MOZART-4 mechanism (Emmons et al.,
118 2010) for the gas-phase chemistry. The MOSAIC (Model for Simulating Aerosol Interactions and Chemistry) aerosol module
119 (Zaveri et al., 2008) is applied for the aerosol chemistry and we represent aerosol particles with 4-size sections having dry
120 diameters ranging from 0.039 μm to 10 μm (Knote et al., 2015). SOA formation is treated with the 1-D volatility basis set
121 (VBS) approach (Donahue et al., 2006) which has been implemented into the MOSAIC aerosol module (Lane et al., 2008a;
122 Ahmadov et al., 2012). Five volatility bins are considered (effective saturation mass concentrations C^* of 10^{-4} , 1, 10, 100,
123 and 1000 $\mu\text{g m}^{-3}$ at 298 K) in the official version 3.7.1 of the WRF-Chem model, with the enthalpy of vaporization (ΔH_{vap})
124 values of 40, 131, 120, 109, and 98 kJ mol^{-1} used in each volatility bin (Knote et al., 2015). We follow Knote et al. (2015)

125 with SOA mass yields adopted for four volatility bins (1, 10, 100, and 1000 $\mu\text{g m}^{-3}$). Further gas-phase aging is simulated
 126 through OH oxidation of SOA vapors with a fixed rate of $1.0 \times 10^{-11} \text{ cm}^3 \text{ molec}^{-1} \text{ s}^{-1}$, with products shifted down one
 127 volatility bin (Murphy and Pandis, 2009), e.g., the condensable vapors with C^* of $1 \mu\text{g m}^{-3}$ react with OH forming surrogate
 128 species in the lowest volatility bin (C^* of $10^{-4} \mu\text{g m}^{-3}$). The partitioning of organic compounds between the gas and particle
 129 phases is simulated based on Pankow (1994) which is implemented in MOSAIC (Shrivastava et al., 2011). We apply glass
 130 transition temperature and viscosity calculations to WRF-Chem model output for traditional SOA formed from the oxidation
 131 of volatile organic compounds including alkanes, alkenes, aromatics, isoprene, and monoterpenes (Lane et al., 2008b).

132 2.2 Glass transition temperature and viscosity calculations

133 The glass-transition temperature of SOA products in each volatility bin at dry conditions ($T_{g,i}$) is calculated as a function of
 134 the saturation mass concentration at 298 K (C^0) using the parameterization (Eq. 1) developed in our previous study (Li et al.,
 135 2020). We assume ideal thermodynamic mixing that C^0 is equal to C^* , which is often applied in the VBS (Donahue et al.,
 136 2011).

$$T_{g,i} = 288.70 - 15.33 \times \log_{10}(C^0) - 0.33 \times [\log_{10}(C^0)]^2 \quad (1)$$

137 The T_g of mixtures of dry SOA compounds ($T_{g,\text{org}}$) is calculated by the Gordon–Taylor equation (Gordon and Taylor,
 138 1952), with the Gordon–Taylor constant (k_{GT}) assumed to be 1 (Dette et al., 2014):

$$T_{g,\text{org}} = \sum_i \omega_i T_{g,i} \quad (2)$$

139 where ω_i is the mass fraction of SOA products in each volatility bin simulated by the VBS module in WRF-Chem.

140 The particle phase state depends strongly on water content in particles, as water can act as a plasticizer to decrease
 141 viscosity (Mikhailov et al., 2009; Koop et al., 2011). The mass concentration of water absorbed by SOA particles under
 142 humid conditions is estimated using the effective hygroscopicity parameter (κ) (Petters and Kreidenweis, 2007) as:

$$m_{\text{H}_2\text{O}} = \left(\frac{a_w}{1 - a_w} \right) \frac{\kappa \rho_w m_{\text{SOA}}}{\rho_{\text{SOA}}} \quad (3)$$

143 where a_w is water activity calculated as $a_w = \text{RH}/100$ and ρ_w is the density of water. m_{SOA} is the simulated total mass
 144 concentrations of traditional SOA. The density of SOA particles (ρ_{SOA}) is assumed to be 1.5 g cm^{-3} (Knote et al., 2015). κ is
 145 assumed to be 0.1 based on previous studies (Gunthe et al., 2009; Duplissy et al., 2011; Wu et al., 2013) and consistent with
 146 the value used in our previous global SOA phase state simulations (Shiraiwa et al., 2017).

147 T_g of organic-water mixtures is also calculated by the Gordon–Taylor equation (Eq. 4) with k_{GT} suggested to be 2.5
 148 (Koop et al., 2011).

$$T_g(\omega_{\text{org}}) = \frac{(1 - \omega_{\text{org}})T_{g,w} + \frac{1}{k_{\text{GT}}} \omega_{\text{org}} T_{g,\text{org}}}{(1 - \omega_{\text{org}}) + \frac{1}{k_{\text{GT}}} \omega_{\text{org}}} \quad (4)$$

149 where ω_{org} is the mass fraction of the simulated SOA species in organic-water mixtures. The glass transition temperature of
 150 pure water ($T_{g,w}$) is 136 K (Kohl et al., 2005). Based on $T_g(\omega_{\text{org}})$, viscosity can be calculated with the
 151 Vogel–Tammann–Fulcher (VTF) equation (Angell, 1991): $\eta = \eta_{\infty} e^{\frac{T_0 D}{T - T_0}}$, where η_{∞} is the viscosity at infinite temperature
 152 (10^{-5} Pa s, Angell (1991)). D is the fragility parameter which is adopted to be 10 based on our previous study in DeRieux
 153 and Li et al. (2018). T_0 is the Vogel temperature calculated as $T_0 = \frac{39.17 T_g(\omega_{\text{org}})}{D + 39.17}$. We further calculate the bulk diffusion
 154 coefficient (D_b) of organic molecules with a radius of 0.4 nm (Maclean et al., 2021) and water molecules in SOA particles
 155 based on predicted viscosity and the fractional Stokes–Einstein equation (Price et al., 2016; Evoy et al., 2019; Evoy et al.,
 156 2020), which is detailed in the Supplement. The mixing timescales of molecules (τ_{mix}) within SOA particles is calculated as
 157 $\tau_{\text{mix}} = d_p^2 / (4\pi^2 D_b)$ (Seinfeld and Pandis, 2016), where d_p is the particle diameter. The d_p is assumed to be 200 nm
 158 (Maclean et al., 2021) when we calculate τ_{mix} .

159 2.3 Sensitivity simulations

160 Table 1 lists all the performed simulations. In the base case, we update the C^* in the lowest volatility bin from $10^{-4} \mu\text{g m}^{-3}$ in
 161 the official WRF-Chem v3.7.1 to $0.1 \mu\text{g m}^{-3}$ based on the ambient volatility observations (referring to Section 2.4 and Fig. 1),
 162 and calculate the ΔH_{vap} in the lowest volatility bin using the semi-empirical parameterization in Epstein et al. (2010), leading
 163 to a value of 142 kJ mol^{-1} . To evaluate the effects of simulated SOA volatility distributions on phase state estimations, we
 164 conduct a simulation (sensitivity case A) following the default setting in the model assuming that the lowest C^* is $10^{-4} \mu\text{g m}^{-3}$
 165 at 298 K, with ΔH_{vap} of 40 kJ mol^{-1} (Knote et al., 2015). A smaller ΔH_{vap} indicates less dependence of volatility on
 166 temperature variations. In the sensitivity case B, we increase the simulated RH by a factor of 10 % as we find that the
 167 simulated RH values are smaller than the observations (Section 3.1). In the base case and sensitivity cases A and B, we
 168 predict T_g for SOA-water mixtures accounting for the SOA-influenced water uptake solely, assuming that SOA particles are
 169 externally mixed with inorganic compounds such as sulfate and nitrate. In the sensitivity case C, we assume that the organic
 170 and inorganic compounds are always internally mixed in one phase and include the water absorbed by inorganic compounds
 171 in viscosity calculations. The water associated with inorganics is calculated by the MOSAIC module coupled in WRF-Chem.

172 2.4 Observation

173 The observation data measured at an urban site in the Institute of Atmospheric Physics (IAP), Chinese Academy of Sciences
 174 ($39^{\circ}58'28''$ N, $116^{\circ}22'16''$ E) in Beijing (Fig. S1 in the Supplement) are used to compare with the simulation results of the
 175 WRF-Chem model. The aerosol volatility was measured from 20 May to 23 June in 2018, using a thermodenuder coupled

176 with an Aerodyne high-resolution aerosol mass spectrometer (Xu et al., 2019). The volatility distributions of oxygenated
177 organic aerosols (OOA) resolved from positive matrix factorization (PMF) were estimated using a dynamic mass transfer
178 model (Riipinen et al., 2010). The volatility of OOA was found to be distributed in six logarithmically spaced C^* bins
179 including 0.001, 0.01, 0.1, 1, 10, and 100 $\mu\text{g m}^{-3}$, based on the best fits between the measured and predicted thermograms
180 using the methods in Karnezi et al. (2014). Chemical species including organics (Org), sulfate (SO_4^{2-}), nitrate (NO_3^-), and
181 ammonium (NH_4^+) in $\text{PM}_{2.5}$ were measured using an Aerodyne time-of-flight aerosol chemical speciation monitor (Fröhlich
182 et al., 2013) equipped with a capture vaporizer and $\text{PM}_{2.5}$ lens, with the details described in Li et al. (2023). The OOA factor
183 was identified with the PMF analysis. We obtain the mass concentrations of $\text{PM}_{2.5}$ from the Olympic Center observation site
184 (<http://zx.bjmemc.com.cn>) which is ~ 4 km from the IAP site (Fig. S1 in the Supplement). Meteorological parameters
185 including RH and T are from the Beijing meteorological tower at the IAP site.

186 3 Results

187 3.1 Simulations in Beijing and the comparison with observations

188 The comprehensive model evaluations were conducted in our previous studies, showing that the WRF-Chem model
189 reasonably captured the magnitudes and spatial distributions of concentrations of major air pollutants over China (Li et al.,
190 2011; Li et al., 2014; Li et al., 2015; Qu et al., 2019; Zhang et al., 2022). Here we focus on the comparison of simulations
191 and observations at the IAP site during 20 May – 23 June 2018 when the observed volatility distributions are available (Xu et
192 al., 2019).

193 Figure 1 shows the average volatility distributions of observed OOA and simulated SOA at the IAP site. The C^* of OOA
194 spans from 0.001 $\mu\text{g m}^{-3}$ to 100 $\mu\text{g m}^{-3}$, with an average value of 1.16 $\mu\text{g m}^{-3}$. The semi-volatile organic compounds (SVOC;
195 $0.3 < C^0 < 300 \mu\text{g m}^{-3}$) and the low-volatile organic compounds (LVOC; $3 \times 10^{-4} < C^0 < 0.3 \mu\text{g m}^{-3}$) (Donahue et al., 2012)
196 contribute 66.3 % and 33.7 % to OOA concentrations, respectively (Xu et al., 2019). The $T_{\text{g,org}}$ estimated from the observed
197 OOA volatility distributions is 286.7 K. Figure 1a shows the simulated volatility distributions of SOA with five C^* bins set to
198 be 0.1, 1, 10, 100, and 1000 $\mu\text{g m}^{-3}$ at 298 K, and ΔH_{vap} of 142, 131, 120, 109, and 98 kJ mol^{-1} used in the five C^* bins,
199 respectively (base case in Table 1). In this base case simulation, the SOA consists of 64.5 % SVOC and 35.3 % LVOC, and
200 most of the SVOC species are located in the C^* bin of 1 $\mu\text{g m}^{-3}$. The simulated SOA in Fig. 1a has an average C^* of 0.64 μg
201 m^{-3} and $T_{\text{g,org}}$ of 291.5 K, close to the values estimated from the volatility distributions of OOA. Figure 1b shows the
202 simulated volatility distributions of SOA with the lowest C^* bin set to be 0.0001 $\mu\text{g m}^{-3}$ at 298 K with ΔH_{vap} of 40 kJ mol^{-1} ,
203 following the default option in the official WRF-Chem model 3.7.1 (Knote et al., 2015). In this sensitivity simulation (case A
204 in Table 1), the SOA consists of 40.4 % extremely low-volatile organic compounds (ELVOC; $C^0 < 3 \times 10^{-4} \mu\text{g m}^{-3}$), which are
205 not determined in the observed OOA, leading to a much lower average C^* (0.03 $\mu\text{g m}^{-3}$) and a higher $T_{\text{g,org}}$ (309.0 K)

206 compared to the observations. In the following we estimate the $T_{g,org}$ and viscosity of SOA using the simulated volatility
207 distributions in the base case with the lowest C^* bin set as $0.1 \mu\text{g m}^{-3}$ at 298 K. The impacts of volatility distributions with
208 the incorporation of ELVOC (Fig. 1b) on viscosity estimations are evaluated in section 3.3.

209 Figure 2 shows that the model relatively well reproduces the observed hourly variations of RH, T , mass concentrations
210 of $\text{PM}_{2.5}$ and its major inorganic components (Figs. 2a – f), with the index of agreement (IOA, defined in the Supplement)
211 varied from ~ 0.70 for inorganic components to a higher value of 0.93 for T (Table S2 in the Supplement). The simulated
212 values of RH are constantly lower than the observations, with the mean bias (MB) being -10.97% (Table S2 in the
213 Supplement). The underestimation of RH observations was also found at other meteorological sites in the North China Plain
214 in our previous studies (Qu et al., 2019; Zhang et al., 2022), which would affect the SOA viscosity estimations. The effects
215 of RH on the viscosity estimations are evaluated in section 3.3. Figure 2g shows that the model could generally reproduce
216 the observed temporal variations of OOA concentrations, but largely underestimates the observation peaks ($\text{MB} = -5.88 \mu\text{g}$
217 m^{-3} , the normalized mean bias $\text{NMB} = -53.28\%$, Table S2 in the Supplement). Incorporation of the SOA formed from
218 intermediate-volatile organic compounds (IVOCs) (Miao et al., 2021; Chang et al., 2022) would increase the simulated SOA
219 concentrations, which is beyond the scope of this study and will be considered in our future work. The simulated SOA mean
220 concentration is $5.15 \mu\text{g m}^{-3}$. Although it is lower than the observed value of $11.03 \mu\text{g m}^{-3}$, this difference in the simulated
221 and observed SOA concentrations would not affect the viscosity predictions significantly. The SOA viscosity has a much
222 closer relation with the volatility rather than its mass loadings (Champion et al., 2019; Li et al., 2020). In our previous study
223 we estimated $T_{g,org}$ and viscosities at different OA mass loadings varied from 1 to $1000 \mu\text{g m}^{-3}$, showing that the simulated
224 viscosities were very similar, particularly when RH was higher than 50% (DeRieux et al., 2018).

225 As the WRF-Chem model underestimates the observed RH at the IAP site, we calculate the SOA viscosity using the
226 simulated and observed RH, respectively. Figure 2h shows that the viscosities calculated at the two conditions are similar at
227 most times during the simulated period, ranging mainly from $\sim 10^2 \text{ Pa s}$ to 10^{10} Pa s , with a median value of $\sim 10^7 \text{ Pa s}$,
228 indicating that a semi-solid phase state frequently occurs. The underestimations of the observed RH by WRF-Chem mainly
229 impact the phase state estimations at relatively high RH. For example, SOA particles occur as liquid when the observed RH
230 is higher than $\sim 75\%$; however, they remain in a semi-solid phase state at the simulated RH. The bulk diffusion coefficients
231 (D_b) of organic molecules range from 10^{-18} to $10^{-11} \text{ cm}^2 \text{ s}^{-1}$ at the simulated RH (Fig. 2i), leading to the mixing timescales
232 within 200 nm SOA particles being seconds to years, with 61% of the time > 1 hour (Fig. S2 in the Supplement). We
233 highlight the mixing timescale of 1 hour as the time step adopted in CTMs is often $\sim 0.5 - 1$ hour (Maclean et al., 2021).
234 Current CTMs usually assume that the gas-particle partitioning of SVOCs reaches equilibrium quickly within the time step
235 (Pankow, 1994; Donahue et al., 2006). When the mixing timescales of organics within SOA particles are $\leq \sim 1$ hour, the
236 instantaneous equilibrium is a reasonable assumption. However, when the mixing timescales of organics are longer than ~ 1
237 hour, non-equilibrium between the gas phase and the particle phase, i.e., the kinetic partitioning may need to be considered in

238 [simulating the SOA formation in CTMs \(Shiraiwa and Seinfeld, 2012; Zaveri et al., 2018; Li and Shiraiwa, 2019; Zaveri et](#)
239 [al., 2020; He et al., 2021; Jathar et al., 2021; Maclean et al., 2021; Shiraiwa and Pöschl, 2021; Shrivastava et al., 2022\).](#)

240 The vertical profiles of SOA viscosity exhibit diurnal variations. Figure 3a shows the median diurnal and vertical
241 profiles of predicted SOA viscosity at the IAP site. The SOA particles remain highly viscous ($\sim 10^7 - 10^8$ Pa s) at the surface,
242 with a higher viscosity occurring from late afternoon to early evening, during which the RH is less than 20 %, lower than the
243 rest time of the day (Fig. S3 [in the Supplement](#)). The SOA particles become more viscous at higher altitudes than the surface
244 and adopt the phase transition from a semi-solid phase to a solid phase at ~ 4 km at the IAP site. The predicted altitude with
245 the phase transition is ~ 2 km higher than our previous global model prediction for the region of East China which was an
246 average of five years' simulations (Shiraiwa et al., 2017). Tan et al. (2020) inferred the phase state of submicrometer
247 particles in Beijing from the surface to an altitude of ~ 1 km using a polarization lidar and found that the particle phase state
248 exhibits a vertical variation. Further observations of SOA viscosity at high altitudes are needed to better understand the
249 viscosity vertical profiles and validate our predictions. Figure 3b shows that the mixing timescales for organic molecules
250 within 200 nm SOA particles are approximately 1 hour at the surface, and longer than ~ 10 hours at altitudes higher than 1
251 km, indicating that kinetic limitations in the gas-particle partitioning may be required to accurately predict SOA mass
252 concentrations in summer Beijing, particularly in the upper planetary boundary layer and the free troposphere.

253 **3.2 Simulated glass transition temperature and viscosity of SOA particles over China**

254 The glass transition temperature of the dry organic phase ($T_{g,org}$) shows a geospatial gradient over China. Figure 4a shows the
255 median surface values of $T_{g,org}$ calculated in the base simulation (Table 1). $T_{g,org}$ ranges from $\sim 287 - 305$ K over most areas of
256 China, with lower values occurring mainly over the southeast and higher values over the northwest. The $T_{g,org}$ range
257 simulated by the WRF-Chem model is consistent with our previous global simulations of $T_{g,org}$ that varied from ~ 285 K to
258 310 K at the surface over China (Shiraiwa et al., 2017). The geospatial variation in $T_{g,org}$ is related to the simulated SOA
259 volatility distributions. Figure 4b shows the mass fractions of SOA species distributed in the lowest volatility bin (SOAX
260 with $C^* = 0.1 \mu\text{g m}^{-3}$ at 298 K). The mass fractions of SOAX are mostly 20 – 35 % in the southeastern China, indicating that
261 the majority of the simulated SOA formed from VOCs is semi-volatile. In these areas, the simulated SOA mass
262 concentrations are higher than the other locations of China (Fig. S4 [in the Supplement](#)) (Li et al., 2022), which is favorable
263 for more SVOCs partitioning into the particle phase, leading to relatively low values of $T_{g,org}$ (Fig. 4a). LVOCs are more
264 frequently contained in aged SOA particles in remote areas, e.g., some areas in the northwestern China where the SOA mass
265 concentrations are very low, resulted in higher $T_{g,org}$ values.

266 The relative humidity plays an important role in regulating SOA viscosity (Koop et al., 2011). Considering the water
267 uptake by SOA particles in the phase state estimations, the predicted geospatial patterns in the viscosity (Fig. 5a) and RH
268 (Fig. S4 [in the Supplement](#)) are very similar with each other, particularly in southern and northeastern China. SOA particles

269 are predicted to mainly be liquid or with a low viscosity ($< 10^4$ Pa s) in the southeast. Figure 5b shows the frequency of
270 liquid phase state, which is calculated as the percent time that an organic aerosol particle is in the liquid phase state during
271 the simulated period. The frequency of liquid particles varies from $\sim 30\%$ to 70% in the southeastern China. The lowest
272 viscosity with the highest frequency of liquid particles occurs over the southern Tibetan Plateau where RH is very high (Fig.
273 S4), which is contributed by summer monsoons and regional moisture recycling (Dong et al., 2016). The SOA particles in
274 the central and northeastern China are predicted to be semi-solid, with the viscosity varied from 10^5 to 10^8 Pa s (Fig. 5a).
275 Highly viscous ($\eta > 10^8$ Pa s) or solid SOA particles are mainly found in the northwest, particularly over the northern Tibetan
276 Plateau where the ambient temperatures are lower than other areas of China (Fig. S4). The frequency of liquid SOA particles
277 in most areas with the latitude higher than 30°N is less than 20% (Fig. 5b).

278 The simulated geospatial pattern in SOA viscosity over China agrees with previous global simulations and ambient
279 measurements. Our previous global simulations predicted a lower viscosity ($\eta < 10^3$ Pa s) in SOA particles in southeastern
280 China and a higher viscosity ($\eta > 10^8$ Pa s) in northwestern China (Shiraiwa et al., 2017; Li et al., 2020), similar to the
281 WRF-Chem simulations in this study. Interestingly, the occurrence of liquid particles over the southern Tibetan Plateau in
282 summer simulated by the WRF-Chem was not found in our previous global predictions, which was an average of five years'
283 simulations (Shiraiwa et al., 2017). The semi-solid phase state of SOA particles simulated in Beijing is consistent with both
284 particle bounce measurements (Liu et al., 2017) and the $\text{PM}_{2.5}$ phase state determined by the poke-and-flow technique (Song
285 et al., 2022). The simulated viscosity of SOA particles is 0.15 Pa s in Shenzhen, a coastal urban city in southeastern China,
286 which also agrees with the findings in the previous bounce measurements indicating that the submicron particles in
287 Shenzhen are in the liquid state (Liu et al., 2019).

288 The phase state of SOA particles is affected by ambient conditions and the particle chemical composition (Koop et al.,
289 2011). Figure 6 shows the median values of viscosity as a function of RH, T and the mass fraction of low-volatility
290 compound (SOAX with C^* of $0.1 \mu\text{g m}^{-3}$ at 298 K) calculated for selected regions in the northern China, southern China,
291 northern Qinghai-Tibet Plateau, and southern Qinghai-Tibet Plateau as specified by white boxes in Fig. 5a. There is a strong
292 inverse relationship between SOA viscosity and relative humidity with high RH ($> \sim 60\%$) as the dominant factor
293 determining the phase state of SOA particles. When RH is lower than $\sim 60\%$, the predicted viscosity is affected by both RH
294 and T . For example, the SOA particles occur mainly as solid over the Northern Qinghai-Tibet Plateau while occur as
295 semi-solid over the Northern China within similar RH ranges ($20\% < \text{RH} < 60\%$); the reason is that the ambient T over the
296 Northern Qinghai-Tibet Plateau is much lower ($\sim 20 \text{ K}$ lower) than the Northern China (Fig. 6b). When RH is relatively low,
297 the viscosity of SOA particles is also influenced by particle chemical composition, i.e., the SOA particles composed of high
298 mass fractions of low volatility compounds tend to have higher viscosity values (Fig. 6c). RH is the main factor driving the
299 diurnal variations of SOA viscosity in our simulations. Figure S5 in the Supplement shows that SOA particles have higher
300 viscosity in the daytime than the nighttime as RH in the daytime is lower than the nighttime (Fig. S6). Compared to the

301 northern China, the southern China exhibits stronger diurnal variations in SOA viscosity that SOA particles occur mainly as
302 semi-solid in the daytime and liquid in the nighttime. Highly viscous or solid SOA particles are found in the northern China
303 during both daytime and nighttime (Fig. S5).

304 The bulk diffusion coefficient is an important parameter determining the mass-transport and mixing rates, which can be
305 predicted by the particle viscosity through the fractional Stokes-Einstein relation (see the Method [section and the](#)
306 [Supplement](#)). The D_b of organic molecules is predicted to be $> \sim 10^{-10} \text{ cm}^2 \text{ s}^{-1}$ in the southern China. The highest value is
307 $\sim 10^{-5} \text{ cm}^2 \text{ s}^{-1}$ occurring in liquid SOA particles in the southern Tibetan Plateau (Fig. 7a) [because of the very low viscosity](#)
308 [simulated over this region \(Fig. 5a\)](#). The D_b of organic molecules within semisolid SOA particles is $\sim 10^{-18} - 10^{-10} \text{ cm}^2 \text{ s}^{-1}$ in
309 the central and northeastern China, and lower than $\sim 10^{-18} \text{ cm}^2 \text{ s}^{-1}$ in highly viscous and solid particles in most areas of the
310 northwestern China. Figure 7b shows the percent time that the mixing timescale of organic molecules in 200 nm particles is
311 less than 1 h in the entire simulation period. The mixing timescale is found nearly always less than 1 h in the southeastern
312 region of the “Hu Huanyong Line”. The “Hu Huanyong Line”, proposed by the Chinese geographer Huanyong Hu, divides
313 China into two parts based on contrasting population densities (Hu, 1935), which was found also useful characterizing the
314 drought conditions, with the northwestern region much dryer than the southeastern region (Zeng et al., 2021). The mixing
315 timescale of organic molecules in highly viscous or solid SOA particles in the northwest of the “Hu Huanyong Line” is often
316 longer than 1 h (the frequency $> 70 \%$), indicating that in these areas kinetic limitations of bulk diffusion should be
317 considered in SOA partitioning. Compared to the diffusion coefficients of organic molecules, the D_b of water molecules in
318 SOA particles at the surface is several orders of magnitude larger, with the values higher than $10^{-10} \text{ cm}^2 \text{ s}^{-1}$ in the southeast,
319 and as low as $\sim 10^{-13} \text{ cm}^2 \text{ s}^{-1}$ in the northwestern China (Fig. 7c). The mixing timescales of water molecules in SOA particles
320 with a diameter of 200 nm are of the order of milliseconds in the southeast and seconds in the northwest of China (Fig. S7 in
321 [the Supplement](#)), indicating that the activation of cloud condensation nuclei would not be inhibited, in agreement with our
322 previous global simulations (Shiraiwa et al., 2017).

323 Figure 8 shows the simulated $T_{g,org}$ and the phase state of SOA particles, as well as the mixing timescale of organic
324 molecules in SOA particles at 500 hPa. The $T_{g,org}$ ranges from $\sim 285 \text{ K} - 295 \text{ K}$, lower than the $T_{g,org}$ simulated at the surface
325 (Fig. 8a). The reason is that the mass fractions of LVOCs (SOAX with C^* of $0.1 \mu\text{g m}^{-3}$ at 298 K) at 500 hPa (Fig. S8 in [the](#)
326 [Supplement](#)) are smaller than the surface values (Fig. 4b). The low temperature at 500 hPa is favorable for SVOCs
327 partitioned into the particle phase, thus compared to the surface conditions, there is less semi-volatile vapors undergoing the
328 further gas-phase aging forming SOAX species. The percent time that an organic aerosol particle is in the liquid phase state
329 (the frequency of liquid SOA particles) at 500 hPa in the southeastern China is 20 – 35 % (Fig. 8b), which is $\sim 20 \%$ lower
330 than the surface values (Fig. 5b). In the northern China, the frequency of liquid SOA particles at 500 hPa is similar to the
331 results at the surface, which is related to the RH spatial patterns (Fig. S9 in [the Supplement](#)). The mixing timescale of
332 organic molecules in 200 nm SOA particles is frequently longer than 1 h at 500 hPa, with the frequency $> 70 \%$ in the

333 northern China and ~ 40 % in the southeastern China (Fig. 8c). The τ_{mix} is relatively short (the frequency of $\tau_{\text{mix}} \leq 1$ h being ~
334 80 %) in some areas of the southwestern China at 500 hPa, where relatively high RH could occur (Fig. S9 in the Supplement)
335 in the season of summer monsoon (Huang et al., 1998).

336 3.3 Sensitivity simulations

337 3.3.1 Impacts of volatility distributions on phase state estimations

338 The volatility and viscosity of organic aerosols are closely related (Rothfuss and Petters, 2017; Shiraiwa et al., 2017;
339 Champion et al., 2019; Zhang et al., 2019b; Li et al., 2020). In this section we conduct sensitivity simulations (case A, Table
340 1) to evaluate how the simulated volatility distributions affect the phase state estimations. The lowest C^* bin in the base case
341 is $0.1 \mu\text{g m}^{-3}$ at 298 K, with ΔH_{vap} of 142 kJ mol^{-1} , which does not incorporate ELVOC species at the room temperature. The
342 sensitivity simulation (case A) adopts the default setting in the official WRF-Chem model v3.7.1, assuming that the lowest
343 C^* is $0.0001 \mu\text{g m}^{-3}$ at 298 K, with ΔH_{vap} of 40 kJ mol^{-1} (Knote et al., 2015). Figure 9a shows that including these ELVOCs at
344 298 K with a relatively small ΔH_{vap} mainly affect the $T_{\text{g,org}}$ simulated over remote areas, e.g., the northwestern China and the
345 marine areas, where the simulated $T_{\text{g,org}}$ is increased by 30 – 40 K. In other regions of China, the changes in $T_{\text{g,org}}$ are less
346 than 25 K. Although consideration of these ELVOCs could affect the simulated $T_{\text{g,org}}$ at the surface obviously in remote areas,
347 i.e., the northwestern China, it does not impact the predicted frequency of the occurrence of a liquid phase state (Fig. 9b), as
348 in these dry areas the SOA particles are highly viscous. Including ELVOC formation at 298 K (ΔH_{vap} of 40 kJ mol^{-1}) mainly
349 affects the phase state estimations in areas with a moderate humidity. For example, in some areas of the southeastern China
350 with ~ 70 % RH, the SOA particles are predicted to be more viscous, with the frequency of a liquid phase state decreasing by
351 up to 12 % (Fig. 9b). These results indicate that the SOA phase state estimations in the base and sensitivity case A are
352 generally in agreement in the simulated episode in this study. Ambient measurements of organic aerosol volatility
353 distributions are still sparse over China. A recent field study showed that the ELVOCs contributed more than half to the OA
354 mass observed at a regional background site near the Bohai Sea (Feng et al., 2023), which resulted in an estimated viscosity
355 much higher than our WRF-Chem simulations. More field volatility distribution measurements should be conducted over
356 China to further evaluate the effects of ELVOCs and how to choose reasonable values of the enthalpy of vaporization that
357 would affect phase state estimations.

358 3.3.2 Impacts of RH and the water absorbed by inorganics on phase state estimations

359 RH is an important parameter affecting the phase state estimations. We perform a sensitivity calculation (case B, Table 1)
360 with the simulated RH increased by a factor of 10 % to compensate for the fact that the current model underestimates the
361 observed RH as shown in Fig. 2 and found in our previous simulations (Qu et al., 2019; Zhang et al., 2022). The increases in
362 simulated RH lead to more occurrence (the liquid frequency increased by 10 – 20 %) of liquid SOA particles in southeastern

363 China where the predicted RH is ranged mainly from 70 to 80 % (Fig. S4 in the Supplement), with very limited effects in
364 phase state predictions in relatively dry areas, e.g., the northern China (Fig. 10a).

365 Besides RH, the mixing state of the organic and inorganic species in atmospheric particles also plays an important role
366 in the phase state of ambient particles. The SOA components are assumed to be phase separated from inorganic compounds
367 in particles in our base simulation, which is consistent to recent ambient observations showing that the phase separation with
368 an organic-rich shell and an inorganic core was a frequent phenomenon in individual particles (diameters > 100 nm)
369 collected over the North China Plain (Li et al., 2021a). To assess the potential effects of inorganic compounds on the phase
370 state of ambient particles, we perform a sensitivity calculation (case C, Table 1) assuming that the organic and inorganic
371 compounds are internally mixed in one phase. In this case the water absorbed by inorganic species can lower the particle
372 viscosity relative to the organic fraction alone. Figure 10b shows that the water associated with inorganic species can
373 significantly lower the viscosity over most areas of China, with the liquid frequency increased by 15 – 45 % in the southeast,
374 and 5 – 15 % in some areas of the northeast. The effects over dry lands in the northwestern China are relatively small.
375 Previous studies showed that at such mixing condition with one phase, on one hand, it is expected that the inorganic salts that
376 often have lower T_g compared to SOA compounds would further lower the particle viscosity (Dette and Koop, 2015). On the
377 other hand, the presence of divalent inorganic ions could increase the viscosity of mixed organic-inorganic particles,
378 enabling a humidity-dependent gel phase transition through cooperative ion-molecule interactions (Richards et al., 2020).
379 For complex mixtures of primary OA, SOA and inorganics, it was found that three distinct phases could occur (Huang et al.,
380 2021). The impacts of the mixing state of organic and inorganic compounds on the phase state of multicomponent particles
381 in ambient air warrant further investigations in future studies (Lilek and Zuend, 2022; Schervish and Shiraiwa, 2023).

382 4 Conclusions

383 We previously developed a new parameterization predicting the glass transition temperature of an organic compound as a
384 function of its volatility (Li et al., 2020). Based on this new parameterization, we use the WRF-Chem model and simulate the
385 T_g and viscosity of SOA particles over China in summer of 2018. This is the first time that spatial and temporal variations in
386 the SOA phase state over China are investigated on a regional scale. The main conclusions are summarized below.

387 (1) Simulations show that T_g values of dry SOA ($T_{g,org}$) range from ~287 K to 305 K over most areas of China at the surface,
388 consistent with our previous simulated results based on a global transport model (Shiraiwa et al., 2017). The $T_{g,org}$ is higher
389 in the northwestern China than the southeastern China. This geospatial variation in $T_{g,org}$ is related to the simulated SOA
390 volatility distributions that SOA particles in northwestern China have relatively low volatilities.

391 (2) Considering the water uptake by SOA particles, the SOA viscosity also shows a prominent geospatial gradient that highly
392 viscous or solid SOA particles are mainly found in the northwestern China. The frequency of liquid SOA particles in most

393 areas with the latitude higher than 30°N is less than 20 %. A very large spatial variation in SOA phase state over the
394 Qinghai-Tibet Plateau was found and we recommend measurements in ambient particle phase state to be conducted over this
395 area, one of the most sensitive regions to climate change.

396 (3) The mixing timescale of organic molecules in 200 nm SOA particles is calculated based on the simulated particle
397 viscosity and the bulk diffusion coefficients of organic molecules. Calculations show that at the surface and at 500 hPa, the
398 percent time of τ_{mix} longer than 1 h is $> \sim 70\%$ in the northwest of the “Hu Huanyong Line”. The implication of this result is
399 that when the τ_{mix} values are greater than roughly 1 h, which is longer than the typical time step in CTMs, the instantaneous
400 equilibrium partitioning usually assumed in SOA formation simulations is subject to be re-evaluated. We recommend to test
401 the effects of kinetic partitioning considering the bulk diffusion in viscous particles on the prediction of SOA mass
402 concentrations and size distributions over the areas with long mixing timescale of organic molecules.

403 (4) The average volatility (C^*) and $T_{\text{g,org}}$ of the simulated SOA agree well with the values estimated from ambient
404 measurements of OOA volatilities at the IAP site in Beijing, where ELVOCs were not determined in the observed OOA (Xu
405 et al., 2019). The sensitivity simulation considering the formation of ELVOCs shows that compared to the base simulation,
406 the frequency of a liquid phase state does not change in most areas of the northern China. In some areas of the southeastern
407 China the SOA particles become more viscous with the percent time that a SOA particle is in the liquid phase state decreases
408 by up to 12 %. It needs more field volatility measurements to evaluate the effects of ELVOCs on OA phase state estimations
409 over China.

410 (5) Differed from the base simulation that SOA components are assumed to be phase separated from inorganic compounds in
411 particles, we conduct a sensitivity simulation assuming that the organic and inorganic compounds are internally mixed in one
412 phase. We show that the water absorbed by inorganic species has a significant impact lowering the simulated viscosity over
413 the southeastern China, with the liquid frequency increased by 15 – 45 %. Future work should consider the effects of the
414 mixing state of organic and inorganic compounds on the prediction of the phase state of multicomponent particles in ambient
415 air.

416 In summary, our simulations demonstrate the spatial distributions of the glass transition temperature and viscosity of
417 SOA particles over China on a regional scale for the first time. The further calculations of the mixing timescale of organic
418 molecules in SOA particles have an implication of the need to evaluate the effects of the phase state on predictions of SOA
419 gas-particle partitioning, and thus the SOA mass concentrations and size distributions in CTMs.

420 *Data availability.* The simulation data in this study are available upon request from the corresponding author
421 (liying-iap@mail.iap.ac.cn).

422 *Supplement.* The supplement related to this article is available on-line.

423 *Author contributions.* YL and MS designed the research. ZZ, HR, and YQ performed the WRF-Chem modeling. ZZ, YL,
424 and HR analyzed the simulation data. WZ, WX, WH, and YS provided observation data. YL, ZZ, and MS wrote the
425 manuscript. ZZ, YL, and HR wrote the supplement. All authors discussed the results and contributed to the article editing.

426 *Competing interests.* At least one of the (co-)authors is a member of the editorial board of Atmospheric Chemistry and
427 Physics. The peer-review process was guided by an independent editor, and the authors have also no other competing
428 interests to declare.

429 *Acknowledgements.* This work was supported by the National Natural Science Foundation of China (grant no. 42075110).
430 The authors thank Qi Chen at the Peking University and Bin Zhao at the Tsinghua University for insightful suggestions on
431 SOA volatility simulations in this work. MS thanks U.S. National Science Foundation for funding (AGS- 2246502).

432 *Financial support.* This work was supported by the National Natural Science Foundation of China (grant no. 42075110).

433 **References**

- 434 Abbatt, J. P. D., Lee, A. K. Y., and Thornton, J. A.: Quantifying trace gas uptake to tropospheric aerosol: recent advances and
435 remaining challenges, *Chem. Soc. Rev.*, 41, 6555-6581, <https://doi.org/10.1039/C2CS35052A>, 2012.
- 436 Ahmadov, R., Mckeen, S. A., Robinson, A. L., Bahreini, R., Middlebrook, A. M., De Gouw, J. A., Meagher, J., Hsie, E. Y.,
437 Edgerton, E., Shaw, S., and Trainer, M.: A volatility basis set model for summertime secondary organic aerosols over
438 the eastern United States in 2006, *J. Geophys. Res.: Atmos.*, 117, <https://doi.org/10.1029/2011JD016831>, 2012.
- 439 Angell, C. A.: Relaxation in liquids, polymers and plastic crystals — strong/fragile patterns and problems, *J. Non-Cryst.*
440 *Solids*, 131-133, 13-31, [https://doi.org/10.1016/0022-3093\(91\)90266-9](https://doi.org/10.1016/0022-3093(91)90266-9), 1991.
- 441 Baboian, V. J., Crescenzo, G. V., Huang, Y., Mahrt, F., Shiraiwa, M., Bertram, A. K., and Nizkorodov, S. A.: Sunlight can
442 convert atmospheric aerosols into a glassy solid state and modify their environmental impacts, *P. Natl. Acad. Sci. USA*,
443 119, e2208121119, <https://doi.org/10.1073/pnas.2208121119>, 2022.
- 444 Champion, W. M., Rothfuss, N. E., Petters, M. D., and Grieshop, A. P.: Volatility and viscosity are correlated in terpene
445 secondary organic aerosol formed in a flow reactor, *Environ. Sci. Technol. Lett.*, 6, 513-519,
446 <https://doi.org/10.1021/acs.estlett.9b00412>, 2019.
- 447 Chang, X., Zhao, B., Zheng, H., Wang, S., Cai, S., Guo, F., Gui, P., Huang, G., Wu, D., Han, L., Xing, J., Man, H., Hu, R.,
448 Liang, C., Xu, Q., Qiu, X., Ding, D., Liu, K., Han, R., Robinson, A. L., and Donahue, N. M.: Full-volatility emission
449 framework corrects missing and underestimated secondary organic aerosol sources, *One Earth*, 5, 403-412,
450 <https://doi.org/10.1016/j.oneear.2022.03.015>, 2022.
- 451 Dalton, A. B. and Nizkorodov, S. A.: Photochemical degradation of 4-nitrocatechol and 2,4-dinitrophenol in a sugar-glass
452 secondary organic aerosol surrogate, *Environ. Sci. Technol.*, 55, 14586-14594, <https://doi.org/10.1021/acs.est.1c04975>,
453 2021.
- 454 DeRieux, W. S. W., Li, Y., Lin, P., Laskin, J., Laskin, A., Bertram, A. K., Nizkorodov, S. A., and Shiraiwa, M.: Predicting the
455 glass transition temperature and viscosity of secondary organic material using molecular composition, *Atmos. Chem.*
456 *Phys.*, 18, 6331-6351, <https://doi.org/10.5194/acp-18-6331-2018>, 2018.
- 457 Dette, H. P. and Koop, T.: Glass formation processes in mixed inorganic/organic aerosol particles, *J. Phys. Chem. A*, 119,
458 4552-4561, <https://doi.org/10.1021/jp5106967>, 2015.
- 459 Dette, H. P., Qi, M., Schröder, D. C., Godt, A., and Koop, T.: Glass-forming properties of 3-methylbutane-1,2,3-tricarboxylic
460 acid and its mixtures with water and pinonic acid, *J. Phys. Chem. A*, 118, 7024-7033,

461 <https://doi.org/10.1021/jp505910w>, 2014.

462 Donahue, N., Robinson, A., Stanier, C., and Pandis, S.: Coupled partitioning, dilution, and chemical aging of semivolatile
463 organics, *Environ. Sci. Technol.*, 40, 2635-2643, <https://doi.org/10.1021/es052297c>, 2006.

464 Donahue, N. M., Epstein, S. A., Pandis, S. N., and Robinson, A. L.: A two-dimensional volatility basis set: 1. organic-aerosol
465 mixing thermodynamics, *Atmos. Chem. Phys.*, 11, 3303-3318, <https://doi.org/10.5194/acp-11-3303-2011>, 2011.

466 Donahue, N. M., Kroll, J. H., Pandis, S. N., and Robinson, A. L.: A two-dimensional volatility basis set – Part 2: Diagnostics
467 of organic-aerosol evolution, *Atmos. Chem. Phys.*, 12, 615-634, <https://doi.org/10.5194/acp-12-615-2012>, 2012.

468 Dong, W., Lin, Y., Wright, J. S., Ming, Y., Xie, Y., Wang, B., Luo, Y., Huang, W., Huang, J., Wang, L., Tian, L., Peng, Y., and
469 Xu, F.: Summer rainfall over the southwestern Tibetan Plateau controlled by deep convection over the Indian
470 subcontinent, *Nat. Commun.*, 7, 10925, <https://doi.org/10.1038/ncomms10925>, 2016.

471 Duplissy, J., Decarlo, P. F., Dommen, J., Alfarra, M. R., Metzger, A., Barmapadimos, I., Prevot, A. S. H., Weingartner, E.,
472 Tritscher, T., Gysel, M., Aiken, A. C., Jimenez, J. L., Canagaratna, M. R., Worsnop, D. R., Collins, D. R., Tomlinson, J.,
473 and Baltensperger, U.: Relating hygroscopicity and composition of organic aerosol particulate matter, *Atmos. Chem.*
474 *Phys.*, 11, 1155-1165, <https://doi.org/10.5194/acp-11-1155-2011>, 2011.

475 Einstein, A.: Über die von der molekularkinetischen Theorie der Wärme geforderte Bewegung von in ruhenden Flüssigkeiten
476 suspendierten Teilchen, 322, 549-560, <https://doi.org/10.1002/andp.19053220806>, 1905.

477 Emmons, L. K., Walters, S., Hess, P. G., Lamarque, J. F., Pfister, G. G., Fillmore, D., Granier, C., Guenther, A., Kinnison, D.,
478 Laepple, T., Orlando, J., Tie, X., Tyndall, G., Wiedinmyer, C., Baughcum, S. L., and Kloster, S.: Description and
479 evaluation of the model for ozone and related chemical tracers, version 4 (MOZART-4), *Geosci. Model Dev.*, 3, 43-67,
480 <https://doi.org/10.5194/gmd-3-43-2010>, 2010.

481 Epstein, S. A., Riipinen, I., and Donahue, N. M.: A semiempirical correlation between enthalpy of vaporization and
482 saturation concentration for organic aerosol, *Environ. Sci. Technol.*, 44, 743-748, <https://doi.org/10.1021/es902497z>,
483 2010.

484 Evoy, E., Kamal, S., Patey, G. N., Martin, S. T., and Bertram, A. K.: Unified description of diffusion coefficients from small
485 to large molecules in organic–water mixtures, *J. Phys. Chem. A*, 124, 2301-2308,
486 <https://doi.org/10.1021/acs.jpca.9b11271>, 2020.

487 Evoy, E., Maclean, A. M., Rovelli, G., Li, Y., Tsimpidi, A. P., Karydis, V. A., Kamal, S., Lelieveld, J., Shiraiwa, M., Reid, J.
488 P., and Bertram, A. K.: Predictions of diffusion rates of large organic molecules in secondary organic aerosols using the
489 Stokes–Einstein and fractional Stokes–Einstein relations, *Atmos. Chem. Phys.*, 19, 10073-10085,
490 <https://doi.org/10.5194/acp-19-10073-2019>, 2019.

491 Fast, J. D., Gustafson Jr, W. I., Easter, R. C., Zaveri, R. A., Barnard, J. C., Chapman, E. G., Grell, G. A., and Peckham, S. E.:
492 Evolution of ozone, particulates, and aerosol direct radiative forcing in the vicinity of Houston using a fully coupled
493 meteorology-chemistry-aerosol model, *J. Geophys. Res.: Atmos.*, 111, <https://doi.org/10.1029/2005JD006721>, 2006.

494 Feng, T., Wang, Y., Hu, W., Zhu, M., Song, W., Chen, W., Sang, Y., Fang, Z., Deng, W., Fang, H., Yu, X., Wu, C., Yuan, B.,
495 Huang, S., Shao, M., Huang, X., He, L., Lee, Y. R., Huey, L. G., Canonaco, F., Prevot, A. S. H., and Wang, X.: Impact
496 of aging on the sources, volatility, and viscosity of organic aerosols in Chinese outflows, *Atmos. Chem. Phys.*, 23,
497 611-636, <https://doi.org/10.5194/acp-23-611-2023>, 2023.

498 Fröhlich, R., Cubison, M. J., Slowik, J. G., Bukowiecki, N., Prévôt, A. S. H., Baltensperger, U., Schneider, J., Kimmel, J. R.,
499 Gonin, M., Rohner, U., Worsnop, D. R., and Jayne, J. T.: The ToF-ACSM: a portable aerosol chemical speciation
500 monitor with TOFMS detection, *Atmos. Meas. Tech.*, 6, 3225-3241, <https://doi.org/10.5194/amt-6-3225-2013>, 2013.

501 Galeazzo, T. and Shiraiwa, M.: Predicting glass transition temperature and melting point of organic compounds via machine
502 learning and molecular embeddings, *Environ. Sci.: Atmos.*, <https://doi.org/10.1039/D1EA00090J>, 2022.

503 Gervasi, N. R., Topping, D. O., and Zuend, A.: A predictive group-contribution model for the viscosity of aqueous organic
504 aerosol, *Atmos. Chem. Phys.*, 20, 2987-3008, <https://doi.org/10.5194/acp-20-2987-2020>, 2020.

505 Gordon, M. and Taylor, J. S.: Ideal copolymers and the second-order transitions of synthetic rubbers. i. non-crystalline
506 copolymers, *J. Appl. Chem.*, 2, 493-500, <https://doi.org/10.1002/jctb.5010020901>, 1952.

507 Grell, G. A., Peckham, S. E., Schmitz, R., Mckeen, S. A., Frost, G., Skamarock, W. C., and Eder, B.: Fully coupled “online”

508 chemistry within the WRF model, *Atmos. Environ.*, 39, 6957-6975, <https://doi.org/10.1016/j.atmosenv.2005.04.027>,
509 2005.

510 Guenther, A. B., Jiang, X., Heald, C. L., Sakulyanontvittaya, T., Duhl, T., Emmons, L. K., and Wang, X.: The Model of
511 Emissions of Gases and Aerosols from Nature version 2.1 (MEGAN2.1): an extended and updated framework for
512 modeling biogenic emissions, *Geosci. Model Dev.*, 5, 1471-1492, <https://doi.org/10.5194/gmd-5-1471-2012>, 2012.

513 Gunthe, S. S., King, S. M., Rose, D., Chen, Q., Roldin, P., Farmer, D. K., Jimenez, J. L., Artaxo, P., Andreae, M. O., Martin,
514 S. T., and Pöschl, U.: Cloud condensation nuclei in pristine tropical rainforest air of Amazonia: size-resolved
515 measurements and modeling of atmospheric aerosol composition and CCN activity, *Atmos. Chem. Phys.*, 9, 7551-7575,
516 <https://doi.org/10.5194/acp-9-7551-2009>, 2009.

517 He, Y., Akherati, A., Nah, T., Ng, N. L., Garofalo, L. A., Farmer, D. K., Shiraiwa, M., Zaveri, R. A., Cappa, C. D., Pierce, J.
518 R., and Jathar, S. H.: Particle size distribution dynamics can help constrain the phase state of secondary organic aerosol,
519 *Environ. Sci. Technol.*, 55, 1466-1476, <https://doi.org/10.1021/acs.est.0c05796>, 2021.

520 Hu, H.: The distribution of China's population, *Acta Geogr. Sin.*, 2, 33-73, <https://doi.org/10.11821/xb193502002>, 1935.

521 Huang, R., Zhang, Z., Huang, G., and Ren, B.: Characteristics of the water vapor transport in east Asian monsoon region and
522 its differences from that of south Asian monsoon region in summer, *Chinese J. Atmospheric Sci.*, 22, 368-379,
523 <https://doi.org/10.3878/j.issn.1006-9895.2003.19204>, 1998.

524 Huang, Y., Mahrt, F., Xu, S., Shiraiwa, M., Zuend, A., and Bertram, A. K.: Coexistence of three liquid phases in individual
525 atmospheric aerosol particles, *P. Natl. Acad. Sci. USA*, 118, e2102512118, <https://doi.org/10.1073/pnas.2102512118>,
526 2021.

527 Jathar, S. H., Cappa, C. D., He, Y., Pierce, J. R., Chuang, W., Billsback, K. R., Seinfeld, J. H., Zaveri, R. A., and Shrivastava,
528 M.: A computationally efficient model to represent the chemistry, thermodynamics, and microphysics of secondary
529 organic aerosols (simpleSOM): model development and application to α -pinene SOA, *Environ. Sci.: Atmos.*, 1, 372-394,
530 <https://doi.org/10.1039/D1EA00014D>, 2021.

531 Jimenez, J. L., Canagaratna, M. R., Donahue, N. M., Prevot, A. S. H., Zhang, Q., Kroll, J. H., Decarlo, P. F., Allan, J. D., Coe,
532 H., Ng, N. L., Aiken, A. C., Docherty, K. S., Ulbrich, I. M., Grieshop, A. P., Robinson, A. L., Duplissy, J., Smith, J. D.,
533 Wilson, K. R., Lanz, V. A., Hueglin, C., Sun, Y. L., Tian, J., Laaksonen, A., Raatikainen, T., Rautiainen, J., Vaattovaara,
534 P., Ehn, M., Kulmala, M., Tomlinson, J. M., Collins, D. R., Cubison, M. J., Dunlea, J., Huffman, J. A., Onasch, T. B.,
535 Alfarra, M. R., Williams, P. I., Bower, K., Kondo, Y., Schneider, J., Drewnick, F., Borrmann, S., Weimer, S., Demerjian,
536 K., Salcedo, D., Cottrell, L., Griffin, R., Takami, A., Miyoshi, T., Hatakeyama, S., Shimono, A., Sun, J. Y., Zhang, Y. M.,
537 Dzepina, K., Kimmel, J. R., Sueper, D., Jayne, J. T., Herndon, S. C., Trimborn, A. M., Williams, L. R., Wood, E. C.,
538 Middlebrook, A. M., Kolb, C. E., Baltensperger, U., and Worsnop, D. R.: Evolution of organic aerosols in the
539 atmosphere, *Science*, 326, 1525, <https://doi.org/10.1126/science.1180353>, 2009.

540 Kanakidou, M., Seinfeld, J. H., Pandis, S. N., Barnes, I., Dentener, F. J., Facchini, M. C., Van Dingenen, R., Ervens, B.,
541 Nenes, A., Nielsen, C. J., Swietlicki, E., Putaud, J. P., Balkanski, Y., Fuzzi, S., Horth, J., Moortgat, G. K., Winterhalter,
542 R., Myhre, C. E. L., Tsigaridis, K., Vignati, E., Stephanou, E. G., and Wilson, J.: Organic aerosol and global climate
543 modelling: a review, *Atmos. Chem. Phys.*, 5, 1053-1123, <https://doi.org/10.5194/acp-5-1053-2005>, 2005.

544 Karnezi, E., Riipinen, I., and Pandis, S. N.: Measuring the atmospheric organic aerosol volatility distribution: a theoretical
545 analysis, *Atmos. Meas. Tech.*, 7, 2953-2965, <https://doi.org/10.5194/amt-7-2953-2014>, 2014.

546 Knopf, D. A. and Alpert, P. A.: Atmospheric ice nucleation, *Nat. Rev. Phys.*, 5, 203-217,
547 <https://doi.org/10.1038/s42254-023-00570-7>, 2023.

548 Knote, C., Hodzic, A., and Jimenez, J. L.: The effect of dry and wet deposition of condensable vapors on secondary organic
549 aerosols concentrations over the continental US, *Atmos. Chem. Phys.*, 15, 1-18, <https://doi.org/10.5194/acp-15-1-2015>,
550 2015.

551 Kohl, I., Bachmann, L., Hallbrucker, A., Mayer, E., and Loerting, T.: Liquid-like relaxation in hyperquenched water at ≤ 140
552 K, *Phys. Chem. Chem. Phys.*, 7, 3210-3220, <https://doi.org/10.1039/B507651J>, 2005.

553 Koop, T., Bookhold, J., Shiraiwa, M., and Pöschl, U.: Glass transition and phase state of organic compounds: dependency on
554 molecular properties and implications for secondary organic aerosols in the atmosphere, *Phys. Chem. Chem. Phys.*, 13,

19238-19255, <https://doi.org/10.1039/C1CP22617G>, 2011.

Kuwata, M. and Martin, S. T.: Phase of atmospheric secondary organic material affects its reactivity, *P. Natl. Acad. Sci. USA*, 109, 17354-17359, <https://doi.org/10.1073/pnas.1209071109>, 2012.

Lane, T. E., Donahue, N. M., and Pandis, S. N.: Effect of NO_x on secondary organic aerosol concentrations, *Environ. Sci. Technol.*, 42, 6022-6027, <https://doi.org/10.1021/es703225a>, 2008a.

Lane, T. E., Donahue, N. M., and Pandis, S. N.: Simulating secondary organic aerosol formation using the volatility basis-set approach in a chemical transport model, *Atmos. Environ.*, 42, 7439-7451, <https://doi.org/10.1016/j.atmosenv.2008.06.026>, 2008b.

Li, J., Han, Z., Wu, J., Tao, J., Li, J., Sun, Y., Liang, L., Liang, M., and Wang, Q. G.: Secondary organic aerosol formation and source contributions over east China in summertime, *Environ. Pollut.*, 306, 119383, <https://doi.org/10.1016/j.envpol.2022.119383>, 2022.

Li, M., Zhang, Q., Kurokawa, J. I., Woo, J. H., He, K., Lu, Z., Ohara, T., Song, Y., Streets, D. G., Carmichael, G. R., Cheng, Y., Hong, C., Huo, H., Jiang, X., Kang, S., Liu, F., Su, H., and Zheng, B.: MIX: a mosaic Asian anthropogenic emission inventory under the international collaboration framework of the MICS-Asia and HTAP, *Atmos. Chem. Phys.*, 17, 935-963, <https://doi.org/10.5194/acp-17-935-2017>, 2017.

Li, W., Liu, L., Zhang, J., Xu, L., Wang, Y., Sun, Y., and Shi, Z.: Microscopic evidence for phase separation of organic species and inorganic salts in fine ambient aerosol particles, *Environ. Sci. Technol.*, 55, 2234-2242, <https://doi.org/10.1021/acs.est.0c02333>, 2021a.

Li, Y. and Shiraiwa, M.: Timescales of secondary organic aerosols to reach equilibrium at various temperatures and relative humidities, *Atmos. Chem. Phys.*, 19, 5959-5971, <https://doi.org/10.5194/acp-19-5959-2019>, 2019.

Li, Y., An, J., and Gultepe, I.: Effects of additional HONO sources on visibility over the North China Plain, *Adv. Atmos. Sci.*, 31, 1221-1232, <https://doi.org/10.1007/s00376-014-4019-1>, 2014.

Li, Y., Carlton, A. G., and Shiraiwa, M.: Diurnal and seasonal variations in the phase state of secondary organic aerosol material over the contiguous US simulated in CMAQ, *ACS Earth Space Chem.*, 5, 1971-1982, <https://doi.org/10.1021/acsearthspacechem.1c00094>, 2021b.

Li, Y., Day, D. A., Stark, H., Jimenez, J. L., and Shiraiwa, M.: Predictions of the glass transition temperature and viscosity of organic aerosols from volatility distributions, *Atmos. Chem. Phys.*, 20, 8103-8122, <https://doi.org/10.5194/acp-20-8103-2020>, 2020.

Li, Y., An, J., Min, M., Zhang, W., Wang, F., and Xie, P.: Impacts of HONO sources on the air quality in Beijing, Tianjin and Hebei Province of China, *Atmos. Environ.*, 45, 4735-4744, <https://doi.org/10.1016/j.atmosenv.2011.04.086>, 2011.

Li, Y., An, J., Kajino, M., Gultepe, I., Chen, Y., Song, T., and Xin, J.: Impacts of additional HONO sources on O₃ and PM_{2.5} chemical coupling and control strategies in the Beijing–Tianjin–Hebei region of China, *Tellus B*, 67, 23930, <https://doi.org/10.3402/tellusb.v67.23930>, 2015.

Li, Z., Xu, W., Zhou, W., Lei, L., Sun, J., You, B., Wang, Z., and Sun, Y.: Insights into the compositional differences of PM₁ and PM_{2.5} from aerosol mass spectrometer measurements in Beijing, China, *Atmos. Environ.*, 301, 119709, <https://doi.org/10.1016/j.atmosenv.2023.119709>, 2023.

Lilek, J. and Zuend, A.: A predictive viscosity model for aqueous electrolytes and mixed organic–inorganic aerosol phases, *Atmos. Chem. Phys.*, 22, 3203-3233, <https://doi.org/10.5194/acp-22-3203-2022>, 2022.

Liu, P., Li, Y. J., Wang, Y., Bateman, A. P., Zhang, Y., Gong, Z., Bertram, A. K., and Martin, S. T.: Highly viscous states affect the browning of atmospheric organic particulate matter, *ACS Cent. Sci.*, 4, 207-215, <https://doi.org/10.1021/acscentsci.7b00452>, 2018.

Liu, Y., Wu, Z., Wang, Y., Xiao, Y., Gu, F., Zheng, J., Tan, T., Shang, D., Wu, Y., Zeng, L., Hu, M., Bateman, A. P., and Martin, S. T.: Submicrometer particles are in the liquid state during heavy haze episodes in the urban atmosphere of Beijing, China, *Environ. Sci. Technol. Lett.*, 4, 427-432, <https://doi.org/10.1021/acs.estlett.7b00352>, 2017.

Liu, Y., Meng, X., Wu, Z., Huang, D., Wang, H., Chen, J., Chen, J., Zong, T., Fang, X., Tan, T., Zhao, G., Chen, S., Zeng, L., Guo, S., Huang, X., He, L., Zeng, L., and Hu, M.: The particle phase state during the biomass burning events, *Sci. Total Environ.*, 792, 148035, <https://doi.org/10.1016/j.scitotenv.2021.148035>, 2021.

602 Maclean, A. M., Butenhoff, C. L., Grayson, J. W., Barsanti, K., Jimenez, J. L., and Bertram, A. K.: Mixing times of organic
603 molecules within secondary organic aerosol particles: a global planetary boundary layer perspective, *Atmos. Chem.*
604 *Phys.*, 17, 13037-13048, <https://doi.org/10.5194/acp-17-13037-2017>, 2017.

605 Maclean, A. M., Li, Y., Crescenzo, G. V., Smith, N. R., Karydis, V. A., Tsimpidi, A. P., Butenhoff, C. L., Faiola, C. L.,
606 Lelieveld, J., Nizkorodov, S. A., Shiraiwa, M., and Bertram, A. K.: Global distribution of the phase state and mixing
607 times within secondary organic aerosol particles in the troposphere based on room-temperature viscosity measurements,
608 *ACS Earth Space Chem.*, 5, 3458-3473, <https://doi.org/10.1021/acsearthspacechem.1c00296>, 2021.

609 Marshall, F. H., Berkemeier, T., Shiraiwa, M., Nandy, L., Ohm, P. B., Dutcher, C. S., and Reid, J. P.: Influence of particle
610 viscosity on mass transfer and heterogeneous ozonolysis kinetics in aqueous–sucrose–maleic acid aerosol, *Phys. Chem.*
611 *Chem. Phys.*, 20, 15560-15573, <https://doi.org/10.1039/C8CP01666F>, 2018.

612 Meng, X., Wu, Z., Guo, S., Wang, H., Liu, K., Zong, T., Liu, Y., Zhang, W., Zhang, Z., Chen, S., Zeng, L., Hallquist, M.,
613 Shuai, S., and Hu, M.: Humidity-dependent phase state of gasoline vehicle emission-related aerosols, *Environ. Sci.*
614 *Technol.*, 55, 832-841, <https://doi.org/10.1021/acs.est.0c05478>, 2021.

615 Miao, R., Chen, Q., Shrivastava, M., Chen, Y., Zhang, L., Hu, J., Zheng, Y., and Liao, K.: Process-based and
616 observation-constrained SOA simulations in China: the role of semivolatile and intermediate-volatility organic
617 compounds and OH levels, *Atmos. Chem. Phys.*, 21, 16183-16201, <https://doi.org/10.5194/acp-21-16183-2021>, 2021.

618 Mikhailov, E., Vlasenko, S., Martin, S. T., Koop, T., and Pöschl, U.: Amorphous and crystalline aerosol particles interacting
619 with water vapor: conceptual framework and experimental evidence for restructuring, phase transitions and kinetic
620 limitations, *Atmos. Chem. Phys.*, 9, 9491-9522, <https://doi.org/10.5194/acp-9-9491-2009>, 2009.

621 Murphy, B. N. and Pandis, S. N.: Simulating the formation of semivolatile primary and secondary organic aerosol in a
622 regional chemical transport model, *Environ. Sci. Technol.*, 43, 4722-4728, <https://doi.org/10.1021/es803168a>, 2009.

623 Pankow, J. F.: An absorption model of gas/particle partitioning of organic compounds in the atmosphere, *Atmos. Environ.*, 28,
624 185-188, [https://doi.org/10.1016/1352-2310\(94\)90093-0](https://doi.org/10.1016/1352-2310(94)90093-0), 1994.

625 Petters, M. D. and Kreidenweis, S. M.: A single parameter representation of hygroscopic growth and cloud condensation
626 nucleus activity, *Atmos. Chem. Phys.*, 7, 1961-1971, <https://doi.org/10.5194/acp-7-1961-2007>, 2007.

627 Pöschl, U. and Shiraiwa, M.: Multiphase chemistry at the atmosphere–biosphere interface influencing climate and public
628 health in the anthropocene, *Chem. Rev.*, 115, 4440-4475, <https://doi.org/10.1021/cr500487s>, 2015.

629 Preston, T. C. and Zuend, A.: Equilibration times in viscous and viscoelastic aerosol particles, *Environ. Sci.: Atmos.*,
630 <https://doi.org/10.1039/D2EA00065B>, 2022.

631 Price, H. C., Mattsson, J., and Murray, B. J.: Sucrose diffusion in aqueous solution, *Phys. Chem. Chem. Phys.*, 18,
632 19207-19216, <https://doi.org/10.1039/C6CP03238A>, 2016.

633 Qu, Y., Chen, Y., Liu, X., Zhang, J., Guo, Y., and An, J.: Seasonal effects of additional HONO sources and the heterogeneous
634 reactions of N₂O₅ on nitrate in the North China Plain, *Sci. Total Environ.*, 690, 97-107,
635 <https://doi.org/10.1016/j.scitotenv.2019.06.436>, 2019.

636 Rasool, Q. Z., Shrivastava, M., Liu, Y., Gaudet, B., and Zhao, B.: Modeling the Impact of the Organic Aerosol Phase State
637 on Multiphase OH Reactive Uptake Kinetics and the Resultant Heterogeneous Oxidation Timescale of Organic Aerosol
638 in the Amazon Rainforest, *ACS Earth Space Chem.*, <https://doi.org/10.1021/acsearthspacechem.2c00366>, 2023.

639 Rasool, Q. Z., Shrivastava, M., Octaviani, M., Zhao, B., Gaudet, B., and Liu, Y.: Modeling volatility-based aerosol phase
640 state predictions in the Amazon Rainforest, *ACS Earth Space Chem.*, 5, 2910-2924,
641 <https://doi.org/10.1021/acsearthspacechem.1c00255>, 2021.

642 Reid, J. P., Bertram, A. K., Topping, D. O., Laskin, A., Martin, S. T., Petters, M. D., Pope, F. D., and Rovelli, G.: The
643 viscosity of atmospherically relevant organic particles, *Nat. Commun.*, 9, 956,
644 <https://doi.org/10.1038/s41467-018-03027-z>, 2018.

645 Richards, D. S., Trobaugh, K. L., Hajek-Herrera, J., Price, C. L., Sheldon, C. S., Davies, J. F., and Davis, R. D.: Ion-molecule
646 interactions enable unexpected phase transitions in organic-inorganic aerosol, *Sci. Adv.*, 6, eabb5643,
647 <https://doi.org/10.1126/sciadv.abb5643>, 2020.

648 Riipinen, I., Pierce, J. R., Donahue, N. M., and Pandis, S. N.: Equilibration time scales of organic aerosol inside

thermodenuders: Evaporation kinetics versus thermodynamics, *Atmos. Environ.*, 44, 597-607, <https://doi.org/10.1016/j.atmosenv.2009.11.022>, 2010.

Roldin, P., Eriksson, A. C., Nordin, E. Z., Hermansson, E., Mogensen, D., Rusanen, A., Boy, M., Swietlicki, E., Svenningsson, B., Zelenyuk, A., and Pagels, J.: Modelling non-equilibrium secondary organic aerosol formation and evaporation with the aerosol dynamics, gas- and particle-phase chemistry kinetic multilayer model ADCHAM, *Atmos. Chem. Phys.*, 14, 7953-7993, <https://doi.org/10.5194/acp-14-7953-2014>, 2014.

Rothfuss, N. E. and Petters, M. D.: Influence of functional groups on the viscosity of organic aerosol, *Environ. Sci. Technol.*, 51, 271-279, <https://doi.org/10.1021/acs.est.6b04478>, 2017.

Schervish, M. and Shiraiwa, M.: Impact of phase state and non-ideal mixing on equilibration timescales of secondary organic aerosol partitioning, *Atmos. Chem. Phys.*, 23, 221-233, <https://doi.org/10.5194/acp-23-221-2023>, 2023.

Schmedding, R., Rasool, Q. Z., Zhang, Y., Pye, H. O. T., Zhang, H., Chen, Y., Surratt, J. D., Lopez-Hilfiker, F. D., Thornton, J. A., Goldstein, A. H., and Vizuete, W.: Predicting secondary organic aerosol phase state and viscosity and its effect on multiphase chemistry in a regional-scale air quality model, *Atmos. Chem. Phys.*, 20, 8201-8225, <https://doi.org/10.5194/acp-20-8201-2020>, 2020.

Seinfeld, J. H. and Pandis, S. N.: *Atmospheric chemistry and physics: from air pollution to climate change*, John Wiley & Sons, 2016.

Shiraiwa, M. and Pöschl, U.: Mass accommodation and gas-particle partitioning in secondary organic aerosols: dependence on diffusivity, volatility, particle-phase reactions, and penetration depth, *Atmos. Chem. Phys.*, 21, 1565-1580, <https://doi.org/10.5194/acp-21-1565-2021>, 2021.

Shiraiwa, M. and Seinfeld, J. H.: Equilibration timescale of atmospheric secondary organic aerosol partitioning, *Geophys. Res. Lett.*, 39, <https://doi.org/10.1029/2012GL054008>, 2012.

Shiraiwa, M., Yee, L. D., Schilling, K. A., Loza, C. L., Craven, J. S., Zuend, A., Ziemann, P. J., and Seinfeld, J. H.: Size distribution dynamics reveal particle-phase chemistry in organic aerosol formation, *P. Natl. Acad. Sci. USA*, 110, 11746, <https://doi.org/10.1073/pnas.1307501110>, 2013.

Shiraiwa, M., Li, Y., Tsimpidi, A. P., Karydis, V. A., Berkemeier, T., Pandis, S. N., Lelieveld, J., Koop, T., and Pöschl, U.: Global distribution of particle phase state in atmospheric secondary organic aerosols, *Nat. Commun.*, 8, 15002, <https://doi.org/10.1038/ncomms15002>, 2017.

Shrivastava, M., Fast, J., Easter, R., Gustafson Jr, W. I., Zaveri, R. A., Jimenez, J. L., Saide, P., and Hodzic, A.: Modeling organic aerosols in a megacity: comparison of simple and complex representations of the volatility basis set approach, *Atmos. Chem. Phys.*, 11, 6639-6662, <https://doi.org/10.5194/acp-11-6639-2011>, 2011.

Shrivastava, M., Rasool, Q. Z., Zhao, B., Octaviani, M., Zaveri, R. A., Zelenyuk, A., Gaudet, B., Liu, Y., Shilling, J. E., Schneider, J., Schulz, C., Zöger, M., Martin, S. T., Ye, J., Guenther, A., Souza, R. F., Wendisch, M., and Pöschl, U.: Tight coupling of surface and in-plant biochemistry and convection governs key fine particulate components over the Amazon Rainforest, *ACS Earth Space Chem.*, 6, 380-390, <https://doi.org/10.1021/acsearthspacechem.1c00356>, 2022.

Shrivastava, M., Cappa, C. D., Fan, J., Goldstein, A. H., Guenther, A. B., Jimenez, J. L., Kuang, C., Laskin, A., Martin, S. T., Ng, N. L., Petaja, T., Pierce, J. R., Rasch, P. J., Roldin, P., Seinfeld, J. H., Shilling, J., Smith, J. N., Thornton, J. A., Volkamer, R., Wang, J., Worsnop, D. R., Zaveri, R. A., Zelenyuk, A., and Zhang, Q.: Recent advances in understanding secondary organic aerosol: implications for global climate forcing, *Rev. Geophys.*, 55, 509-559, <https://doi.org/10.1002/2016RG000540>, 2017.

Song, M., Jeong, R., Kim, D., Qiu, Y., Meng, X., Wu, Z., Zuend, A., Ha, Y., Kim, C., Kim, H., Gaikwad, S., Jang, K.-S., Lee, J. Y., and Ahn, J.: Comparison of phase states of PM_{2.5} over megacities, Seoul and Beijing, and their implications on particle size distribution, *Environ. Sci. Technol.*, <https://doi.org/10.1021/acs.est.2c06377>, 2022.

Song, Y. C., Haddrell, A. E., Bzdek, B. R., Reid, J. P., Bannan, T., Topping, D. O., Percival, C., and Cai, C.: Measurements and predictions of binary component aerosol particle viscosity, *J. Phys. Chem. A*, 120, 8123-8137, <https://doi.org/10.1021/acs.jpca.6b07835>, 2016.

Tan, W., Li, C., Liu, Y., Meng, X., Wu, Z., Kang, L., and Zhu, T.: Potential of polarization lidar to profile the urban aerosol phase state during haze episodes, *Environ. Sci. Technol. Lett.*, 7, 54-59, <https://doi.org/10.1021/acs.estlett.9b00695>,

696 2020.

697 Tong, Y.-K., Liu, Y., Meng, X., Wang, J., Zhao, D., Wu, Z., and Ye, A.: Relative humidity-dependent viscosity of single quasi
698 aerosol particle and possible implications for atmospheric aerosol chemistry, *Phys. Chem. Chem. Phys.*,
699 <https://doi.org/10.1039/D2CP00740A>, 2022.

700 Wu, Z. J., Poulain, L., Henning, S., Dieckmann, K., Birmili, W., Merkel, M., Van Pinxteren, D., Spindler, G., Müller, K.,
701 Stratmann, F., Herrmann, H., and Wiedensohler, A.: Relating particle hygroscopicity and CCN activity to chemical
702 composition during the HCCT-2010 field campaign, *Atmos. Chem. Phys.*, 13, 7983-7996,
703 <https://doi.org/10.5194/acp-13-7983-2013>, 2013.

704 Xu, W., Xie, C., Karnezi, E., Zhang, Q., Wang, J., Pandis, S. N., Ge, X., Zhang, J., An, J., Wang, Q., Zhao, J., Du, W., Qiu, Y.,
705 Zhou, W., He, Y., Li, Y., Li, J., Fu, P., Wang, Z., Worsnop, D. R., and Sun, Y.: Summertime aerosol volatility
706 measurements in Beijing, China, *Atmos. Chem. Phys.*, 19, 10205-10216, <https://doi.org/10.5194/acp-19-10205-2019>,
707 2019.

708 Zaveri, R. A., Easter, R. C., Fast, J. D., and Peters, L. K.: Model for Simulating Aerosol Interactions and Chemistry
709 (MOSAIC), *J. Geophys. Res.: Atmos.*, 113, <https://doi.org/10.1029/2007JD008782>, 2008.

710 Zaveri, R. A., Easter, R. C., Shilling, J. E., and Seinfeld, J. H.: Modeling kinetic partitioning of secondary organic aerosol
711 and size distribution dynamics: representing effects of volatility, phase state, and particle-phase reaction, *Atmos. Chem.*
712 *Phys.*, 14, 5153-5181, <https://doi.org/10.5194/acp-14-5153-2014>, 2014.

713 Zaveri, R. A., Shilling, J. E., Zelenyuk, A., Zawadowicz, M. A., Suski, K., China, S., Bell, D. M., Veghte, D., and Laskin, A.:
714 Particle-phase diffusion modulates partitioning of semivolatile organic compounds to aged secondary organic aerosol,
715 *Environ. Sci. Technol.*, 54, 2595-2605, <https://doi.org/10.1021/acs.est.9b05514>, 2020.

716 Zaveri, R. A., Wang, J., Fan, J., Zhang, Y., Shilling, J. E., Zelenyuk, A., Mei, F., Newsom, R., Pekour, M., Tomlinson, J.,
717 Comstock, J. M., Shrivastava, M., Fortner, E., Machado, L. a. T., Artaxo, P., and Martin, S. T.: Rapid growth of
718 anthropogenic organic nanoparticles greatly alters cloud life cycle in the Amazon rainforest, *Sci. Adv.*, 8, eabj0329,
719 <https://doi.org/10.1126/sciadv.abj0329>, 2022.

720 Zaveri, R. A., Shilling, J. E., Zelenyuk, A., Liu, J., Bell, D. M., D'ambro, E. L., Gaston, C. J., Thornton, J. A., Laskin, A., Lin,
721 P., Wilson, J., Easter, R. C., Wang, J., Bertram, A. K., Martin, S. T., Seinfeld, J. H., and Worsnop, D. R.: Growth kinetics
722 and size distribution dynamics of viscous secondary organic aerosol, *Environ. Sci. Technol.*, 52, 1191-1199,
723 <https://doi.org/10.1021/acs.est.7b04623>, 2018.

724 Zeng, P., Sun, F., Liu, Y., Wang, Y., Li, G., and Che, Y.: Mapping future droughts under global warming across China: a
725 combined multi-timescale meteorological drought index and SOM-Kmeans approach, *Weather Clim. Extreme*, 31,
726 100304, <https://doi.org/10.1016/j.wace.2021.100304>, 2021.

727 Zhang, J., Lian, C., Wang, W., Ge, M., Guo, Y., Ran, H., Zhang, Y., Zheng, F., Fan, X., Yan, C., Daellenbach, K. R., Liu, Y.,
728 Kulmala, M., and An, J.: Amplified role of potential HONO sources in O₃ formation in North China Plain during
729 autumn haze aggravating processes, *Atmos. Chem. Phys.*, 22, 3275-3302, <https://doi.org/10.5194/acp-22-3275-2022>,
730 2022.

731 Zhang, Y., Chen, Y., Lei, Z., Olson, N. E., Riva, M., Koss, A. R., Zhang, Z., Gold, A., Jayne, J. T., Worsnop, D. R., Onasch, T.
732 B., Kroll, J. H., Turpin, B. J., Ault, A. P., and Surratt, J. D.: Joint impacts of acidity and viscosity on the formation of
733 secondary organic aerosol from isoprene epoxydiols (IEPOX) in phase separated particles, *ACS Earth Space Chem.*, 3,
734 2646-2658, <https://doi.org/10.1021/acsearthspacechem.9b00209>, 2019a.

735 Zhang, Y., Niehman, L., Spencer, P., Jung, J. I., Lee, A., Heffernan, B. K., Gold, A., Zhang, Z., Chen, Y., Canagaratna, M. R.,
736 Jayne, J. T., Worsnop, D. R., Onasch, T. B., Surratt, J. D., Chandler, D., Davidovits, P., and Kolb, C. E.: The cooling
737 rate- and volatility-dependent glass-forming properties of organic aerosols measured by broadband dielectric
738 spectroscopy, *Environ. Sci. Technol.*, 53, 12366-12378, <https://doi.org/10.1021/acs.est.9b03317>, 2019b.

739 Zheng, B., Tong, D., Li, M., Liu, F., Hong, C., Geng, G., Li, H., Li, X., Peng, L., Qi, J., Yan, L., Zhang, Y., Zhao, H., Zheng,
740 Y., He, K., and Zhang, Q.: Trends in China's anthropogenic emissions since 2010 as the consequence of clean air actions,
741 *Atmos. Chem. Phys.*, 18, 14095-14111, <https://doi.org/10.5194/acp-18-14095-2018>, 2018.

742 Ziemann, P. J. and Atkinson, R.: Kinetics, products, and mechanisms of secondary organic aerosol formation, *Chem. Soc.*

743
744
745
746
747
748
749
750
751
752
753
754
755
756
757
758
759
760
761
762
763
764
765
766
767
768
769
770

771 **Table 1.** Sensitivity calculations for evaluating the effects of simulated SOA volatility distributions (sensitivity case A), RH (sensitivity
772 case B) and the water absorbed by inorganic components (sensitivity case C) on viscosity estimations.

773

Cases	C^* at 298 K and ΔH_{vap} in each volatility bin	The liquid water content considered in viscosity estimations	RH
Base case	0.1, 1, 10, 100, and 1000 $\mu\text{g m}^{-3}$ with ΔH_{vap} of 142, 131, 120, 109, and 98 kJ mol^{-1}	water absorbed by SOA particles with the assumption that SOA particles are externally mixed with inorganics	RH simulated by WRF-Chem
Sensitivity case A	0.0001, 1, 10, 100, and 1000 $\mu\text{g m}^{-3}$ with ΔH_{vap} of 40, 131, 120, 109, and 98 kJ mol^{-1}	water absorbed by SOA particles with the assumption that SOA particles are externally mixed with inorganics	RH simulated by WRF-Chem
Sensitivity case B	0.1, 1, 10, 100, and 1000 $\mu\text{g m}^{-3}$ with ΔH_{vap} of 142, 131, 120, 109, and 98 kJ mol^{-1}	water absorbed by SOA particles with the assumption that SOA particles are externally mixed with inorganics	RH simulated by WRF-Chem increased by a factor of 10%
Sensitivity case C	0.1, 1, 10, 100, and 1000 $\mu\text{g m}^{-3}$ with ΔH_{vap} of 142, 131, 120, 109, and 98 kJ mol^{-1}	water absorbed by both SOA particles and inorganic components with the assumption that SOA particles are internally mixed with inorganics	RH simulated by WRF-Chem

774

775

776

777

778

779

780

781

782

783

784

785

786

787

788

789

790

791

792

793

794

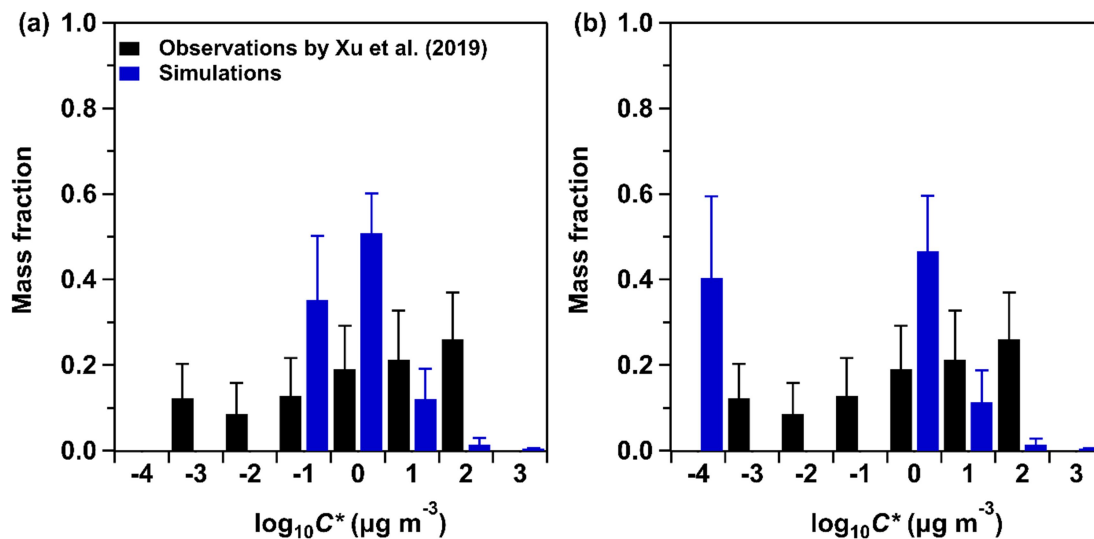
795

796

797

798

799



800

801 **Figure 1.** Comparison of the average volatility distributions of observed OOA and simulated SOA at the IAP site during 20 May – 23 June
 802 2018. The black bars represent the volatility distributions of observed OOA adopted from Xu et al. (2019). The blue bars represent the
 803 volatility distributions of SOA simulated by WRF-Chem, with five C^* bins set to be 0.1, 1, 10, 100, and 1000 $\mu\text{g m}^{-3}$ at 298 K in (a), and
 804 0.0001, 1, 10, 100, and 1000 $\mu\text{g m}^{-3}$ at 298 K in (b). The blue error bars represent the one standard deviation.

805

806

807

808

809

810

811

812

813

814

815

816

817

818

819

820

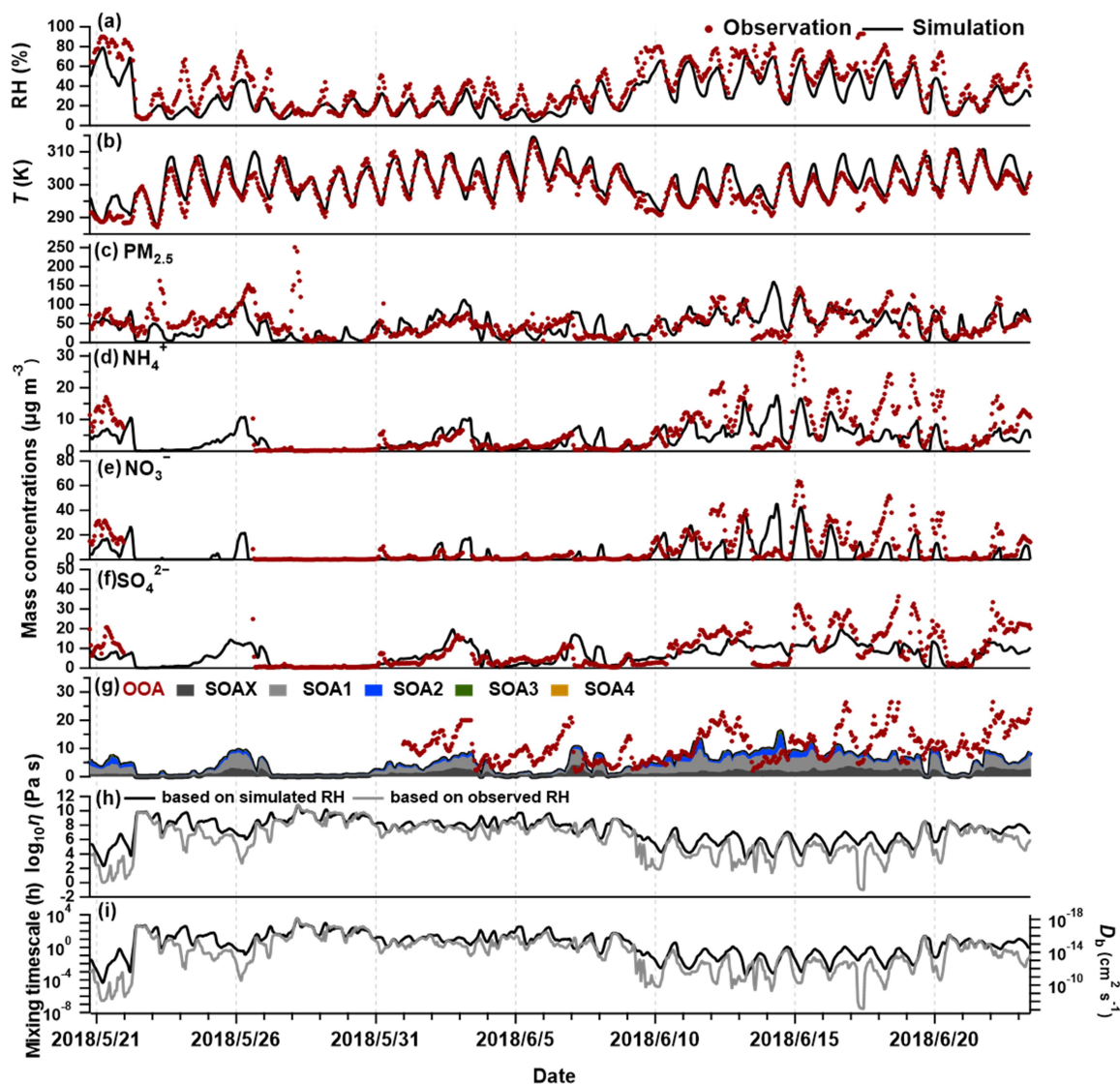
821

822

823

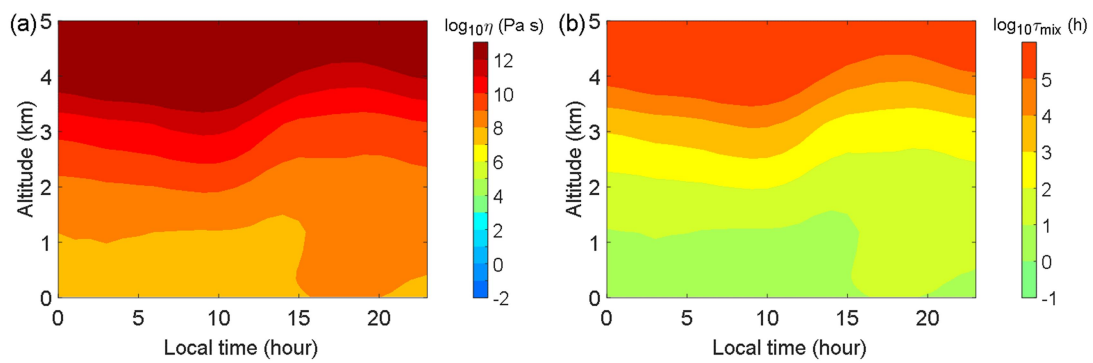
824

825



826
 827 **Figure 2.** Observations and simulations of temporal variations of (a) RH, (b) T , (c) $\text{PM}_{2.5}$ concentrations, (d) NH_4^+ concentrations, (e)
 828 NO_3^- concentrations, and (f) SO_4^{2-} concentrations at the IAP site. (g) Observed OOA concentrations (red dots) and simulated SOA
 829 concentrations, with SOAX, SOA1, SOA2, SOA3, and SOA4 represent the SOA with C^* of 0.1, 1, 10, 100, and 1000 $\mu\text{g m}^{-3}$ at 298 K,
 830 respectively. (h) SOA viscosity, and (i) bulk diffusion coefficients and mixing timescale of organic molecules within 200 nm SOA particles
 831 calculated using the RH simulated by the WRF-Chem model or the RH observed at the IAP site.

832
 833
 834
 835
 836
 837



838

839 **Figure 3.** Median diurnal and vertical profiles of estimated (a) SOA viscosity and (b) mixing timescales for organic molecules within 200
 840 nm SOA particles at the IAP site during May 20 – June 23 in 2018. Note: altitude is approximate and estimated from WRF pressure layers.

841

842

843

844

845

846

847

848

849

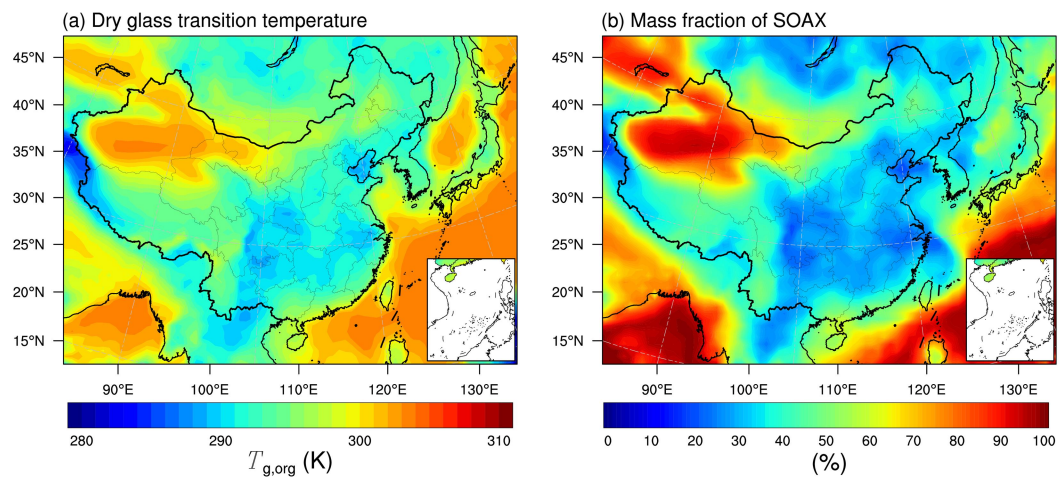
850

851

852

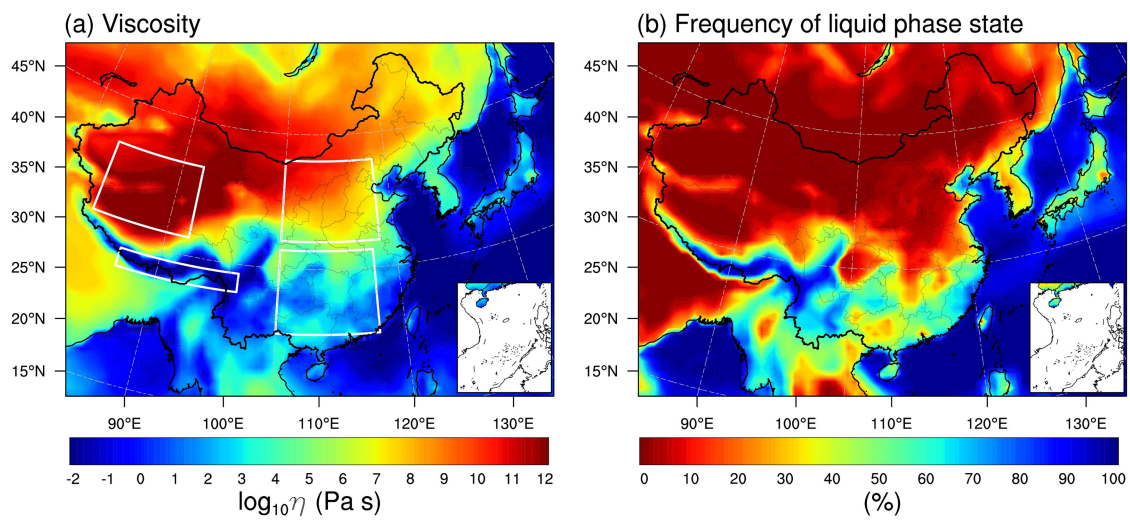
853

854



855
 856 **Figure 4.** The predicted median surface values of (a) glass transition temperature of SOA particles at the dry condition and (b) mass
 857 fractions of SOAX ($C^* = 0.1 \mu\text{g m}^{-3}$ at 298 K) during May 20 – June 23 in 2018 simulated in the base case (Table 1).

858
 859
 860
 861
 862
 863
 864
 865
 866
 867
 868
 869
 870
 871



872

873 **Figure 5.** WRF-Chem predicted (a) median surface values of viscosity and (b) the percent time that an organic aerosol particle is in the
 874 liquid phase state during May 20 – June 23 in 2018. The white boxes in panel (a) specify the selected regions in the northern China,
 875 southern China, northern Qinghai-Tibet Plateau, and southern Qinghai-Tibet Plateau.

876

877

878

879

880

881

882

883

884

885

886

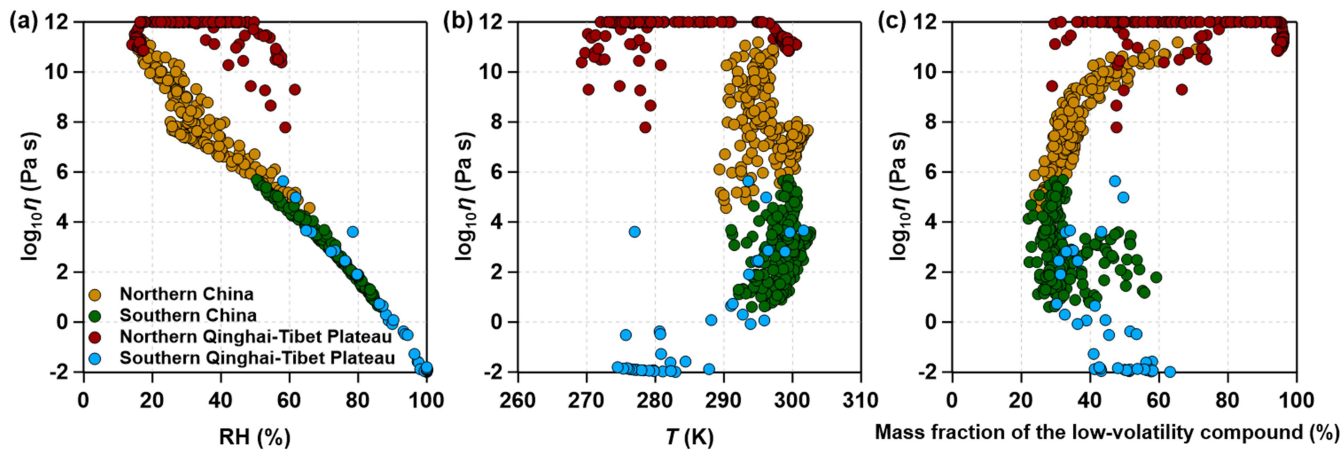
887

888

889

890

891



892

893 **Figure 6.** The median values of viscosity as a function of (a) RH, (b) T and (c) the mass fraction of SOAX ($C^* = 0.1 \mu\text{g m}^{-3}$ at 298 K)
 894 calculated for selected regions in the northern China, southern China, northern Qinghai-Tibet Plateau, and southern Qinghai-Tibet Plateau
 895 as specified by white boxes in Fig. 5a during May 20 – June 23 in 2018.

896

897

898

899

900

901

902

903

904

905

906

907

908

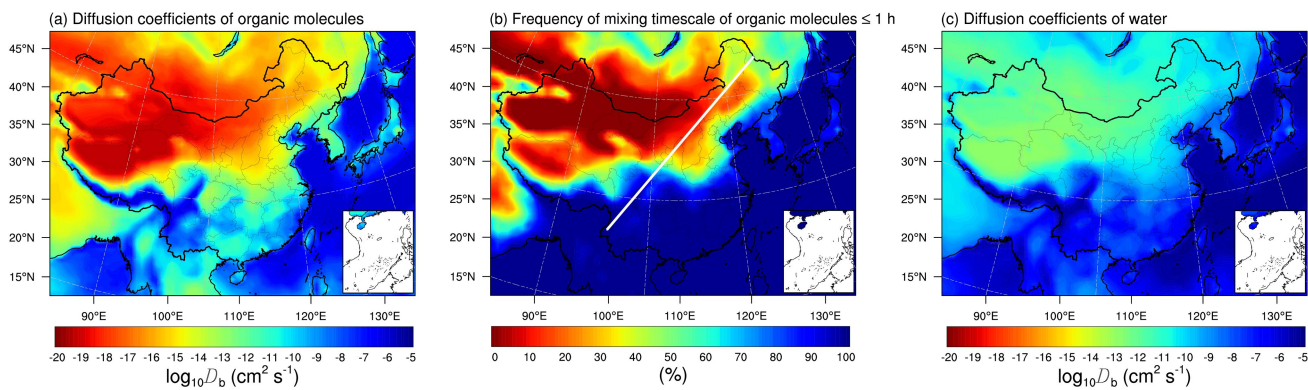
909

910

911

912

913



914

915 **Figure 7.** WRF-Chem predicted median surface values of the diffusion coefficients of (a) organic molecules and (c) water molecules in
 916 SOA particles. (b) The percent time that the mixing timescale of organic molecules in a 200 nm particle is less than 1 h during May 20 –
 917 June 23 in 2018. The white line indicates the “Hu Huanyong Line” (Hu, 1935).

918

919

920

921

922

923

924

925

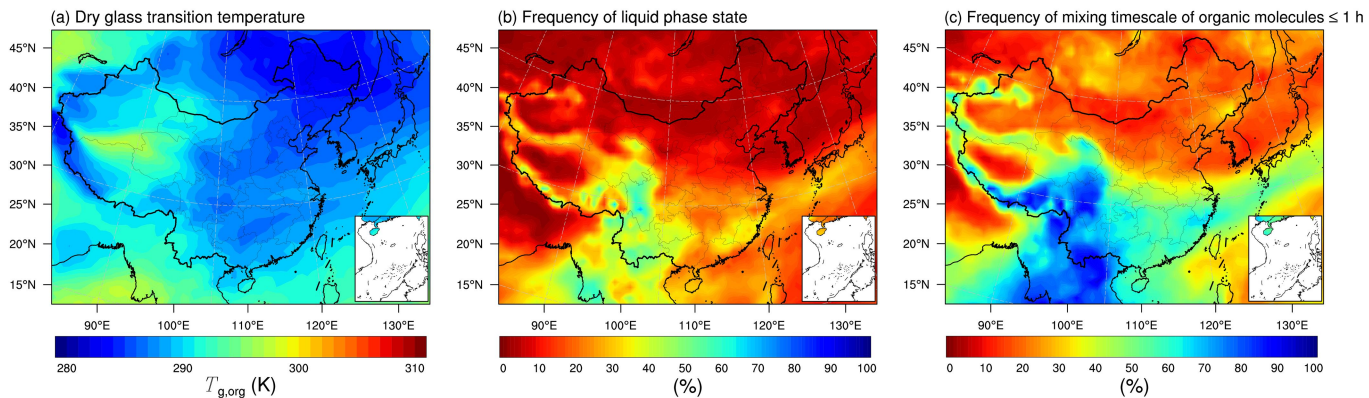
926

927

928

929

930



931

932 **Figure 8.** WRF-Chem predicted median values of (a) glass transition temperature of SOA particles at the dry condition, (b) the percent
 933 time that an organic aerosol particle is in the liquid phase state, and (c) the percent time that the mixing timescale of organic molecules in a
 934 200 nm particle is less than 1 h at 500 hPa during May 20 – June 23 in 2018.

935

936

937

938

939

940

941

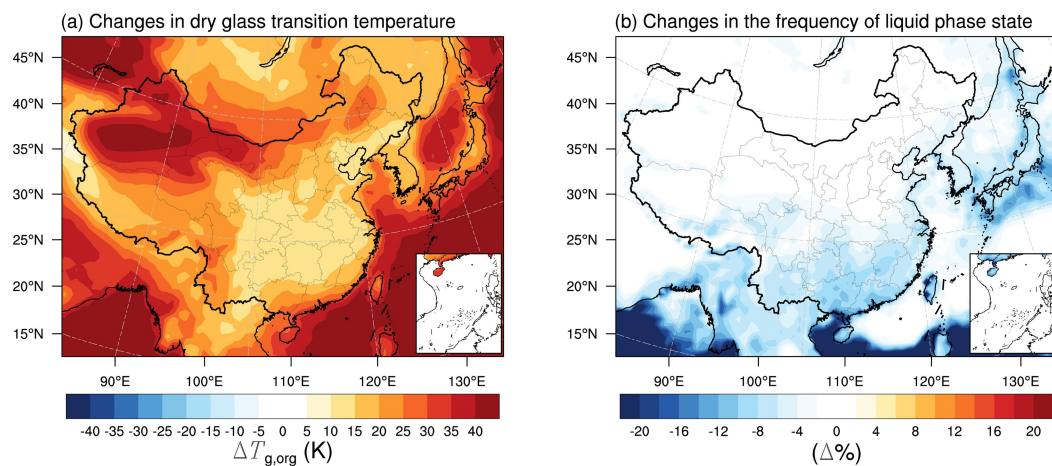
942

943

944

945

946



947

948 **Figure 9.** Modelled median differences of (a) glass transition temperature of SOA particles at the dry condition, and (b) the percent time
 949 that an organic aerosol particle is in the liquid phase state between a sensitivity case with the lowest C^* of $0.0001 \mu\text{g m}^{-3}$ at 298 K (ΔH_{vap} of
 950 40 kJ mol^{-1} , case A in Table 1) and a base case with the lowest C^* of $0.1 \mu\text{g m}^{-3}$ at 298 K (ΔH_{vap} of 142 kJ mol^{-1} , Table 1).

951

952

953

954

955

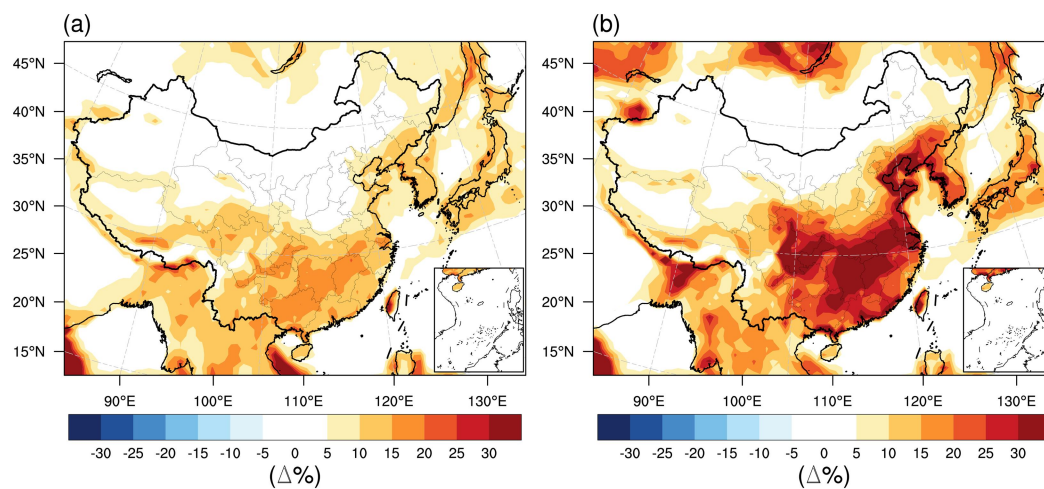
956

957

958

959

960



961
 962 **Figure 10.** (a) Impacts of RH on the percent time that an organic aerosol particle is in the liquid phase state: modelled median differences
 963 between a case with the WRF-Chem simulated RH increased by a factor of 10 % (case B, Table 1) and a base case (Table 1) with the
 964 WRF-Chem simulated RH. (b) Impacts of the water absorbed by inorganics on the percent time that an organic aerosol particle is in the
 965 liquid phase state: modelled median differences between a case considering the water absorbed by both SOA particles and inorganics (case
 966 C, Table 1) and a base case (Table 1) considering the water absorbed by SOA particles solely.

967
 968